The beamline ID32 at the ESRF for soft X-ray high energy resolution resonant inelastic X-ray scattering and polarisation dependent X-ray absorption spectroscopy

N.B. Brookes [a,*], F. Yakhou-Harris [a], K. Kummer [a], A. Fondacaro [a], J.C. Cezar [a,1], D. Betto [a], E. Velez-Fort [a], A. Amorese [a,2], G. Ghiringhelli [b,c], L. Braicovich [a,b], R. Barrett [a], G. Berruyer [a] F. Cianciosi [a], L. Eybert [a], P. Marion [a], P. van der Linden [a,d], L. Zhang [a,3]

[a] *ESRF, The European Synchrotron, 71 Avenue des Martyrs, F-38043 Grenoble, France*
[b] *Dipartimento di Fisica, Politecnico di Milano, Piazza Leonardo da Vinci 32, I-20133 Milano, Italy*
[c] *CNR-SPIN, Dipartimento di Fisica, Politecnico di Milano, Piazza Leonardo da Vinci 32, I-20133 Milano, Italy*
[d] *Partnership for Soft Condensed Matter (PSCM), 71 avenue des Martyrs, Grenoble, France*

Keywords:
Synchrotron radiation
Soft X-ray beam line
RIXS
XMCD
VLS-PGM
Spectrometer

The ID32 Soft X-ray Beamline line is an ESRF upgrade beamline for X-ray absorption (XAS) and Resonant Inelastic X-ray Scattering (RIXS) spectroscopic studies. It was opened to Users in October 2014 and provides polarised soft X-rays in the 400–1600 eV energy range. It has two branches: One branch has been designed for X-ray magnetic dichroism experiments, both linear (XMLD) and circular (XMCD), with high sensitivity, reproducibility, flexibility, user friendliness and the capability for fast energy scanning. The X-ray beam is available in two experimental areas, one with a dedicated superconducting high field magnet and a sample preparation facility, the second area being open for User instruments. The other branch is dedicated to very high energy resolution Resonant Inelastic X-ray Scattering experiments with a combined resolving power up to 30 000 around 930 eV. A scattering arm which is continuously variable under UHV vacuum over 100 degrees and a four-circle sample goniometer allows accurate positioning of the sample to enable 3D mapping of q space. Combined with the possibility of polarisation analysis of the outgoing photons the beamline provides a state-of-the-art soft X-ray RIXS facility.

1. Introduction

As part of the phase I ESRF Upgrade several new beamlines were constructed [1]. In the soft X-ray range a new beamline (ID32) dedicated to very high energy resolution soft X-ray Resonant Inelastic X-ray Scattering (RIXS) and soft X-ray dichroism (XMCD/XMLD) was developed. The design of the beamline and the results of commissioning will be presented. The possible future evolution of the beamline will also be addressed.

XMLD and XMCD measurements need certain characteristics of the beamline to be optimised. The beamline covers the energy range 400–1600 eV and the source needs to provide full control of the light polarisation both circular and linear polarised. The energy range allows absorption edges to be scanned from the nitrogen and oxygen K-edges (400–550 eV) through the 3d transition metal (Ti–Cu) $L_{2,3}$, edges (450–1000 eV) as well as the 4f rare-earth (Ce–Yb) $M_{4,5}$ edges (880–1600 eV). These elements typically make up many of the important magnetic materials and their absorption edges are particularly important since they correspond to 2p–3d for the 3d metals and 3d–4f transitions for the rare-earths, meaning that the empty electronic states responsible for the magnetism are directly probed [2]. To efficiently carry out such studies the beamline should be able to easily cover the entire energy range and allow fast scans across any absorption edge (typically 90–180 s for a 100 eV scan). Since difference spectra are taken, very good stability (position and energy) and normalisation with an I0 intensity monitor is also needed. On the other hand the energy resolution required from the

* Corresponding author.
E-mail address: brookes@esrf.fr (N.B. Brookes).
[1] Current Address: Brazilian Synchrotron Light Laboratory (LNLS) - Brazilian Center for Research in Energy and Materials (CNPEM) - CP 6192 - Campinas - SP - Brazil - 13083-970.
[2] Max Planck Institute for Chemical Physics of Solids, Nöthnitzer Straße 40, 01187 Dresden, Germany.
[3] Stanford University, SLAC National Accelerator Laboratory, Menlo Park, United States.

Table 1
List of optical components for the common (upper panel), XMCD branch (middle panel) and the RIXS branch (lower panel). The quoted values are the measured ones.

Double Mirror and monochromator pre-mirror	M1	M2	Pre-mirror (PM)
Distance from source (m)	29.949	30.560	~64.2415
Shape	Flat	Toroid	Flat
Tangential radius (km)	−44.4	4.571	~276
Sagittal radius (m)	>100	0.2137	–
Dimension (L × W × H) mm^3	260 × 60 × 100	260 × 60 × 100	450 × 120 × 100
Angle of incidence (deg.)	0.75	0.75	1.5 to 2.5
Coating	B_4C	B_4C	B_4C and Au
Roughness (Å rms)	2.0	2.6	2.0
Substrate material	Silicon	Silicon	Silicon
Slope error (μrad rms)	0.31	0.5	0.1
Manufacturer	SESO/Winlight	SESO/Winlight	Zeiss

XMCD branch	300 l/mm Grating (G)	900 l/mm Grating (G)	Deflecting mirror (DFM)	Horizontally Refocusing Mirror (HRM)	Vertically Refocusing Mirror (VRM)	Refocusing Plane Mirror (RPM)
Distance (m)	64.456	64.456	65.956	116.500	117.600	117.950
Shape	Flat	Flat	Cylinder	Elliptical (bender)	Elliptical (bender)	Flat
Tangential radius (km)	>−70	>−70	71	Mean radius 0.413	Mean radius 0.1617	76
Sagittal radius (m)	–	–	0.4967	–	–	–
Dimension (L × W × H) mm^3	200 × 40 × 30	200 × 40 × 30	260 × 50 × 25	300 × 50 × 15	300 × 50 × 15	200 × 50 × 40
Angle of incidence (deg.)	0.9 to 2.35	0.9 to 2.0	1.0	1.25	2.0	2.0
Coating	Pt	Pt	Pt	Pt	B_4C and Pt	B_4C and Pt
Roughness (Å rms)	1–1.5	1–1.5	1.2	0.66	0.7/1.9	5
Material	Silicon	Silicon	Silicon	Silicon	Silicon	Silicon
Slope error (μrad rms)	0.12–0.14	0.12–0.14	1.1	0.28	0.22	0.51/0.25
Manufacturer	Zeiss/DIOS	Zeiss/DIOS	SESO	Coastline Optics	Coastline Optics	SESO

RIXS branch	Grating 800 l/mm (G)	Grating 1600 l/mm (G)	Vertically refocusing mirror (VRM)	Horizontally Refocusing mirror (HRM)
Distance (m)	64.456	64.456	108.3	108.65
Shape	Flat	Flat	Elliptical (bender)	Sagittal cylinder
Tangential radius (km)	>−70	>−70	Mean radius 0.1617	219
Sagittal radius (m)	–	–	–	0.05134
Dimension (L × W × H) mm^3	200 × 40 × 30	200 × 40 × 30	300 × 50 × 15	200 × 50 × 45
Angle of incidence (deg.)	0.7 to 1.4	1.0 to 1.9	1.114	1.114
Coating	Au	Au	Pt	Au
Roughness (Å rms)	1–1.5	1–1.5	<1	5.7
Material	Silicon	Silicon	Silicon	Silicon
Slope error (μrad rms)	0.12–0.14	0.12–0.14	0.22	0.27
Manufacturer	Zeiss/Shimadzu	Zeiss/Shimadzu	Coastline Optics	Zeiss

XMCD branch of the beamline is not too demanding and is sufficient if less than the energy width due to the core-hole lifetime. This also means that a small variation in the energy resolution across an absorption scan is not an issue. Typically a resolving power ($E/\Delta E$) of 5000 is sufficient for most XMCD studies. The current beamline meets these needs and in addition provides an easy way of adjusting the beam size at the sample. A small focus is useful in studying small samples, while studies of X-ray sensitive samples (e.g. some single molecular magnets) benefit from a large spot which reduces the flux density. The current beamline achieves this by providing bendable mirrors focusing independently in both the horizontal and vertical plane.

Another goal of this XMCD branch was to provide beam to another experimental area located behind the main XMCD end-station. This area has no fixed end-station and is to accommodate User end stations or special set-ups for new types of experiments. The bendable mirrors also allow the beam to be focused in this experimental area and provide the same beam quality as for the normal XMCD end-station.

Resonant Inelastic scattering experiments are photon-in photon-out experiments [2,3]. The light is scattered from the sample and the energy of the scattered photons is measured with a spectrometer after the sample. The technique is very flux hungry and the general tendency is to move to very high energy resolution with the possibility of measuring over a wide range of scattering angles, which gives information about the momentum transfer of the photons. The aim for the new ESRF beamline was to have a combined resolving power (beamline + spectrometer) of 30 000 at the Cu L-edge at 932 eV, with a continuous range of scattering angles from 150 to 50 degrees. The resulting instrument would have 2–3 times better resolution than the best instrument so far [4–6]. The experiments typically use linear polarised light, both vertical and horizontal. The energy range covers the L edges of the 3d transition metals from 400–1000 eV (Ti–Cu), the oxygen K edge at 520 eV and the rare-earth $M_{4,5}$ edges from 900–1500 eV.

Consequently, although the energy range for the two branches are similar and both need a variable polarised undulator source there are distinct differences in the needs of the two branches which the current beamline has had to address.

2. Beamline layout and optical components

In designing the ID32 soft X-ray beamline several factors had to be taken into account. Firstly, there should be two branches accommodating both XMCD and RIXS experiments as described above. In addition, several strategic choices were made: the beam height was chosen to be ~1.4 m and the beam was kept in the horizontal plane for ease of use. Optical choices like sagittal focusing with horizontally deflecting optics were also made for stability reasons. Having a long beamline (~100–120 m) allowed for a large RIXS spectrometer (~12 m) and to well separate the two branches. The required space became possible with the new experimental hall built as part of the ESRF Upgrade I as shown in Fig. 1. The two branches are separated using a deflecting mirror (DFM)

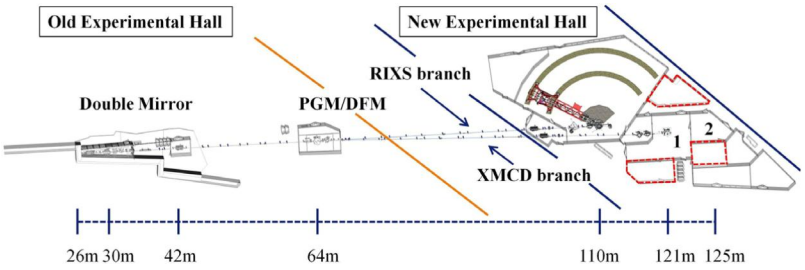

Fig. 1. ID32 beamline floor plan – the component distances are given from the centre of the ID32 straight section. The control cabins are outlined by red dashed lines.

Table 2
Undulator parameters.

APPLE II helical undulator	HU88A &C	HU88B
Magnetic material	NdFeB	NdFeB
Bz max. field (T)	0.6	0.6
Bx max. field (T)	0.55	0.55
Length (m)	1.6	2.5
Period (mm)	88	88
Phase: Linear 0-90 degrees (mm)	0–44	0–44
Phase: Circular (mm)	23–32	23–32
Minimum gap (mm)	16	16
Flux (@900 eV): Circ. Pol. (Ph/sec/0.1%BW/200 mA)	4.5×10^{14}	9.7×10^{14}

after the Plane Grating Monochromator (PGM) chamber. Due to the soft X-ray energy range (400–1600 eV) the beamline is windowless from the X-ray source to the sample.

After a discussion of the source properties, the various optical components are described below. The beamline optics common to the two branches are discussed first followed by the XMCD and RIXS branches. The beamline diagnostic tools are then discussed followed by a concluding section with future prospects. The optical layout for the two branches is shown schematically in Fig. 2 and the components are listed in Table 1. The quoted values for the various parameters are the measured ones.

3. Undulator source

Since the beamline needs to cover RIXS and XMCD applications the X-ray source should have tuneable polarisation with both linear and circular polarised light. In addition for the RIXS experiment, a flux hungry technique, a very intense source is needed. This has led to the ID32 6 m straight section being equipped with three APPLE-II [7,8] NdFeB permanent magnet helical undulators with an 88 mm period.

In the centre of the straight section there is a 2.5 m device (HU88B), with two 1.6 m long devices (HU88A & C) upstream and downstream. The magnetic parameters are given in Table 2.

The undulators provide horizontal linear (in the plane of the ring: 0°), vertical linear (90°) and circularly polarised light over the energy range 400 eV to 1600 eV. Only the first harmonic is used and the degree of polarisation is close 100% at all energies and for all polarisations. The linear polarisation from the 1.6 m long undulators can be rotated 0° to 90°. The linear polarisation from the 2.5 m device can be rotated from −90° to +90°.

The vertical source size and divergence changes with the undulator length (e.g. 1.6 or 2.5 m) and the photon energy. It varies from approx. 31 μm to 13 μm and 11 to 21 μrad (rms) respectively. In the horizontal plane the source size (rms) is around 412 μm and the divergence varies from approx. 16 μrad to 33 μrad (rms) [9]. By working with a monochromator entrance slit one can keep a constant source size in the vertical plane.

The beamline is aligned on the undulator axis using a DiagOn [10] beam viewer positioned immediately before the first optical element (M1, Fig. 2). A typical false colour 2D intensity map is shown in Fig. 3.

The beam viewer works with a diffracted beam at 45° from a water cooled Si[111]. The undulator 1st harmonic is typically set at ~1400 eV. Then the off-axis radiation at ~2.8 keV from the undulator is seen as a ring on the viewer. The primary slits can then be centred on the ring and the beamline aligned to this position.

The alignment can be performed independently for all three undulators and any vertical misalignment can be corrected by correctors in the undulator straight section [11].

The beam viewer crystal is simply inserted into the beam for alignment and removed during normal operation. See Desjardins et al. 2007 [10] for further details.

4. Optics common to both branches

4.1. Double mirror

The double mirror device is comprised of horizontally deflecting plane (M1) and toroidal (M2) mirrors, both at 0.75° incidence angle and in a ± configuration i.e. the two mirrors face each other. The mirror dimensions and achieved parameters are given in Table 1 (upper panel). The mirrors were fabricated by SESO.

The outgoing beam is parallel to the incoming beam and offset horizontally by 16 mm. This allows the positioning of a tungsten heavy metal Bremsstrahlung stop in line with the straight through beam after the toroidal mirror. The offset X-ray beam is taken through a 10 ×6 mm^2 (Horizontal (H) ×Vertical (V)) aperture. The toroid focuses the beam in the vertical plane at the monochromator entrance slit located 42 m from the source (see Fig. 2: Optical Layout) and collimates in the horizontal plane. The two mirrors are mounted on a hexapod support, giving six degrees of freedom [12]. In addition the toroidal mirror can be rotated independently about the vertical axis (z) ±150 μrad, mainly to adjust the parallelism of the mirrors. This is done using an in-vacuum piezo activator with an in-vacuum capacitive sensor (PI). Vacuum in the chamber is kept to less than 2 x 10^{-9} mbar, using an ion pump and two flange mounted getter pumps giving a total pumping speed of 1400 l/s. The mirrors are coated with Boron Carbide (B_4C) which has a high reflectivity for the energy range of interest but absorbs the unwanted high energies reducing the heat load on the entrance slit and monochromator optics. In the worse case the M1 mirror will absorb ~1 kW of power. Consequently much care was taken in the cooling design to minimise distortions of the optical surface. Using finite element analysis, the incidence angle, mirror substrate shape, and water cooling configuration were optimised to minimise the impact of the thermal load at this location. A smart-cut design [13] was used for the mirror cooling with a top-side cooling scheme. Finite element calculations showed that the main effect would be on the horizontal beamsize at the sample. By choosing to overfill the mirror and select the part of the mirror transmitting beam to the beamline using secondary slits, the effect on the beam size can be minimised. Typically a 2.5 mm horizontal aperture secondary slit can be used which transmits most of the intensity.

An additional problem encountered due to the heat load is the development of a contamination track. In addition, contamination of iron, chromium and nickel was observed which probably came from

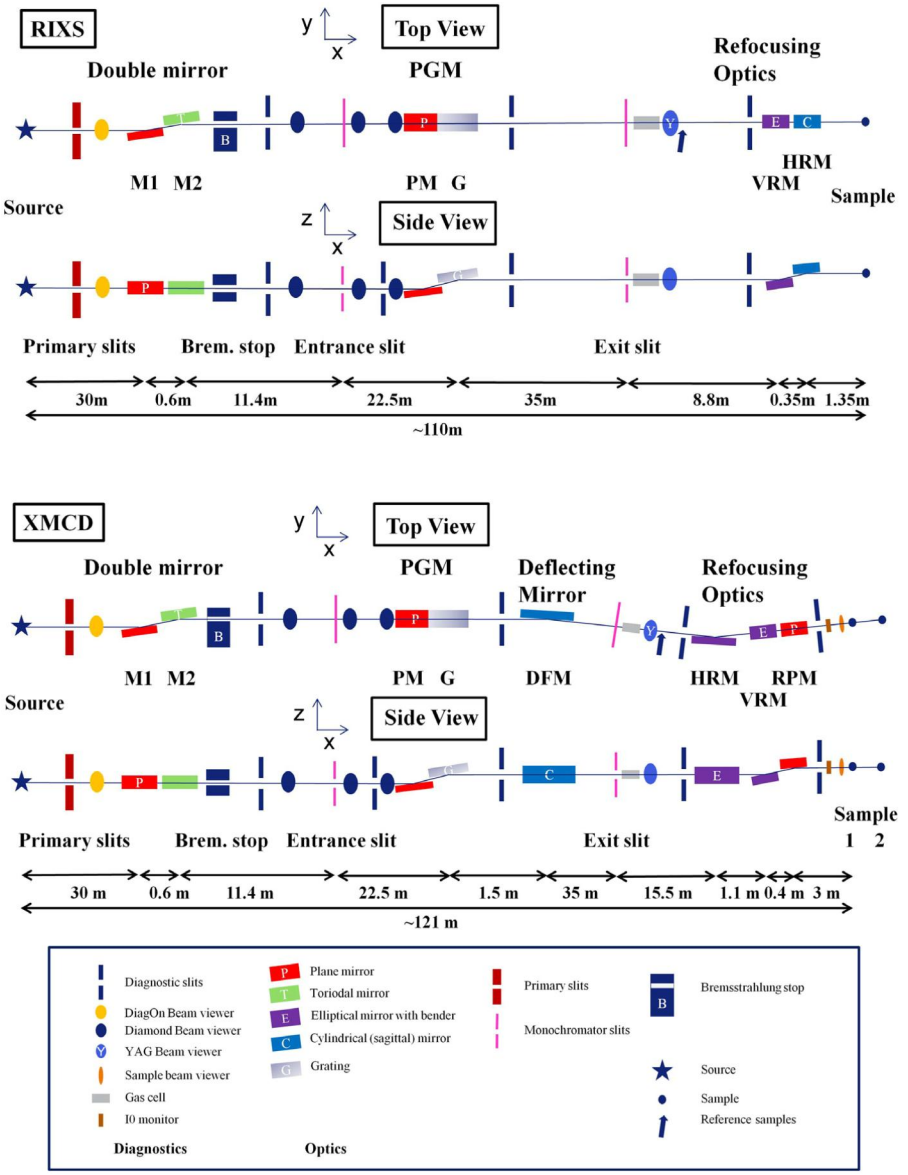

Fig. 2. ID32 beamline optical layout. Upper and lower panels show the RIXS and XMCD branches respectively.

the B_4C coating or the chromium binding layer. Attempts to remove the carbon contamination using oxygen dosing, as has been successfully used in the monochromator (see Section 4.2.2), led to an erosion of the mirror surface. Even after recoating, which removed the main metallic contaminants, a loss of reflectivity due to the roughness of the surface remained. Consequently, the mirrors were replaced with mirrors from Winlight which were coated in-house. The B_4C coating was applied directly to the mirror without a chromium binder. The problem of metal contamination was solved and the reflectivity improved.

4.2. *Plane grating monochromator*

The plane grating monochromator (PGM) is composed of an entrance slit, a plane mirror, variable line spacing (VLS) plane gratings, a horizontally deflecting cylindrical mirror for the XMCD branch and separate exit slits for each branch (Fig. 2). The pressure at the position of all the main components is $< 2 \times 10^{-9}$ mbar. Although the monochromator is common to the two branches the optical schemes are different as will be described below. The common parts are the entrance slit, the monochromator plane mirror and the mechanics which will be described first.

4.2.1. *The entrance slit*

The entrance slit is at the vertical focus of the M2 mirror – the source point being the middle of the undulator straight section. The slit is typically set to a 30 μm vertical aperture which transmits most of the intensity. Due to the high power density in the vertical plane the cooling had to be carefully optimised. The beam is approx. 2000 μm ×30 μm (H ×V) Full Width Half Maximum (FWHM) with a maximum power of ~27 W. The slit assembly is water cooled and was manufactured by TOYAMA. The entrance slit can move +/−300 mm along the beam direction to facilitate the initial alignment but during operation it is fixed. The slit can also be scanned in the vertical plane to profile the beam and can be rotated about the beam direction to allow the slit to be set parallel to the monochromator optical elements. The blades are made of tungsten.

4.2.2. *Monochromator mechanics and pre-mirror*

The PGM monochromator mechanics (Fig. 4) was provided by BESTEC, based on a classic SX700 design [14] with a pre-mirror facing up and four gratings facing down in a fixed-exit setup with a 15 mm beam offset upwards. The pre-mirror rotation axis is shifted from the grating axis so that the beam reflected by the mirror always hits the

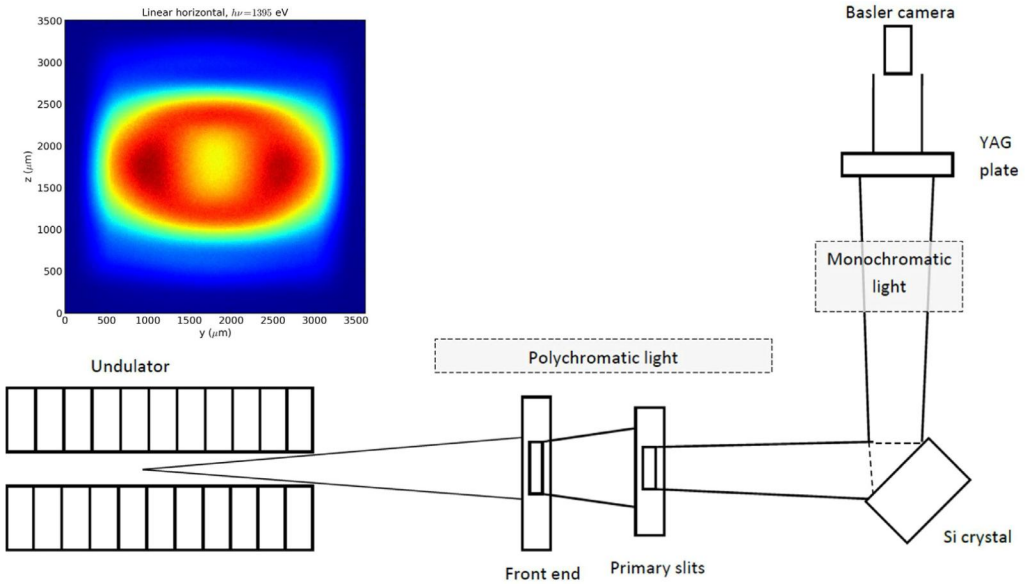

Fig. 3. The false colour image shows the DiagOn image of the undulator with the first harmonic of the undulator at ~1400 eV. The sketch shows the layout of the device used on ID32.

centre of the grating within a few μm, while the beam footprint moves along the mirror depending on the incident angle. The length of the mirror (here 450 mm) is then determined by the chosen offset and the working angular range.

The mirror and gratings cradle (Fig. 4) separate rotations are actuated via a sine-bar mechanism and encoded with high resolution in-vacuum rotational encoders with two readheads per axis (Renishaw RESM 206 mm diameter 20 μm pitch rings, TONIC DSi units). The achieved minimal incremental motion and stability for the grating rotation is 0.01 μrad and 0.008 μrad over 4 h respectively, as demonstrated during the factory acceptance tests. Two high precision translation stages allow for grating and/or mirror strip selection.

The mechanics are enclosed in a 900 mm inner diameter chamber installed on a high stability granite support with a motorised fine height adjustment to allow for vertical beam tracking. The supporting feet that connect the internal mechanics with the adjustable frame are mechanically decoupled from the chamber walls.

The plane mirror was fabricated by Zeiss featuring two strips with a B_4C or gold coating. Since the two coatings have different cut-off energies this is used to reduce higher order contamination of the beam. The mirror design used a new concept for this monochromator and was developed in collaboration between the ESRF team and BESTEC. The new feature is that the mirror is liquid nitrogen cooled. Finite element analysis of the distortion of the optical shape due to the heat load from the beam, showed that to maintain the slope error in an acceptable range, water cooling was not sufficient. By keeping the mirror at around 123 K, which corresponds to approximately zero for the thermal expansion coefficient of silicon [15,16] the slope error can be kept to a level that does not impact on the energy resolution of the instrument. In order to optimise the cooling and reduce possible vibrations, the shape and size of the mirror, the mirror support and the cooling configuration were optimised. The Silicon mirror is cross shaped and 100 mm thick, see Fig. 4. Silicon pads were inserted between the coolers and the sides of the mirror to minimise deformation during the cooling down process. Ceramic heaters placed on the pads allow the temperature to be regulated. In normal operation the mirror is stabilised at ~130 K which is a compromise between the heating and cooling circuits.

Since the target energy resolution of the beamline is achieved, it follows that the slope error must be kept within an acceptable level and proves that the cooling scheme works well. One disadvantage of liquid nitrogen cooling is that carbon contamination rapidly grows on the mirror as seen previously [17]. Following earlier work [18] it is found that by dosing the mirror with a small flow of oxygen gas (10^{-9} mbar range) the carbon is "burnt off" by the X-ray beam and stays clean as long as the gas flow is maintained. No degradation of the optical surface has been observed.

Following the mirror, the grating is mounted facing down (Fig. 4). Four grating slots are available. This is needed as the same mechanics serves both the XMCD and RIXS branch lines of the beamline and both have a high flux and a high resolution grating each. The grating blanks were fabricated by Zeiss. The gratings are selected by an in-vacuum translation stage perpendicular to the beam (Fig. 4). The gratings are individually water cooled. Most importantly the whole grating kinematic support with the mounted grating and cooling circuit can be removed as a unit for each grating separately. This allows the mounted grating to be checked in the optics laboratory in order to avoid optical distortions. The clamping of the optics and the mounting of the cooling circuit can strongly modify the intrinsic slope error of the optics. Preservation of the slope error is essential as this is a major factor in determining the energy resolution.

5. XMCD branch

5.1. XMCD optical concept

For the XMCD branch the beamline monochromator uses an optical concept first described by Howells and Staub [19] and later used by Pereiro et al. [20]. This scheme has not been used for a soft X-ray dichroism beamline before but has several advantages. For XMCD experiments we need to rapidly scan (continuous scans) the monochromator over an absorption edge and also easily change energy over the entire working range of the beamline. Having the possibility of only scanning the grating while the pre-mirror angle is fixed facilitates this. However, being able to choose different pre-mirror angles to maximise efficiency or harmonic rejection and still be able to just scan the grating for measurements gives a very flexible set-up. The current design also means that the exit slit is fixed in position and since the energy resolution varies slowly over an absorption edge the slit opening can also be fixed. This is all achieved by using a VLS grating and adjusting the line spacing parameters to give a fixed virtual focus at a distance equal to the grating entrance slit distance (r_1) and then refocusing this image at the exit slit [19]. In our case the refocusing is done with the cylindrical sagittally focusing mirror after the grating. The virtual focus at the entrance slit

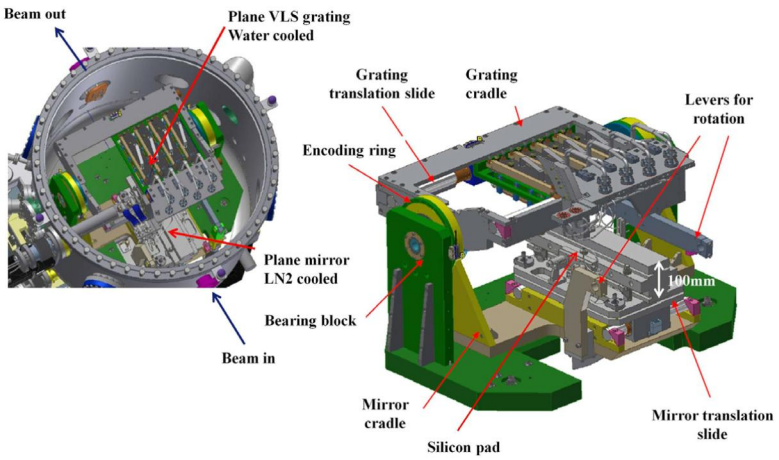

Fig. 4. Internal components of the PGM chamber (courtesy of BESTEC).

can be achieved using a very simple relationship for the VLS grating parameters [19,20]:

$$D(w) = a_0(1 - (2/r_1)w + (3/(r_1 * r_1))w^2 + \cdots) = a_0 + a_1 w + a_2 w^2 + \ldots..$$

Where $D(w)$ is the line density along the beam direction and $w = 0$ is the centre of the grating and a_0 is the line density at the centre of the grating, r_1 the entrance arm length (in our case the entrance slit to grating distance) and the positive direction is towards the exit slit.

The required resolving power (5000) is obtained with a 300 l/mm grating and an entrance arm length (r_1) of 22 456 mm and $a_0 = +300$ l/mm, giving:

$$a_1 = -2 * a_0/r_1 = -0.02672 \text{ l/mm}^2 \text{ and}$$
$$a_2 = 3 * a_0/(r_1 * r_1) = +1.785 \times 10^{-6} \text{ l/mm}^3$$

A second 900 l/mm grating gives a much higher energy resolution (>10 000 over the entire energy range) and since the dispersion is higher an improved insensitivity to angular changes is also achieved. This can be important for measuring very small dichroism effects. The required resolving power is easily obtained with an entrance arm length (r1) of 22 456 mm and $a_0 = +900$ l/mm, giving:

$$a_1 = -2 * a_0/r_1 = -0.08016 \text{ l/mm}^2 \text{ and}$$
$$a_2 = 3 * a_0/(r_1 * r_1) = +5.354 \times 10^{-6} \text{ l/mm}^3$$

Note that the sign of the terms are + − +. Higher terms are not needed.

It should be noted that the line density varies in the opposite direction to conventional systems since the objective is to produce a divergent beam with a virtual source at a distance $r_2 = -r_1$. With a range of pre-mirror angles from at least 1.5° to 2.5° and the 400–1600 eV range of the beamline the grating is always in focus so the pre-mirror angle can be fixed and only the grating scanned to perform an energy scan. With a pre-mirror angle of 2° the entire energy range can be covered by a simple rotation of the grating.

For continuous scans (0.2–1 eV/s) only the grating needs to be rotated from the start energy to the end energy. This is done continuously measuring the encoder to give the energy at each point. Typically the undulator gap is scanned simultaneously with the monochromator to have an approximately constant flux across the scan. All other parameters are fixed.

5.2. XMCD components

5.2.1. XMCD grating parameters

The gratings were made by DIOS and the BESSY II synchrotron. The final measured grating parameters are shown in Table 3.

The gratings were mechanically ruled and blazed to give a high efficiency over the entire working range of the beamline. Fig. 5 shows the calculated efficiency using the REFLEC program [21] for the 300 l/mm grating with fixed included (grazing) angles of 175° (2.5°), 176° (2°) and 177° (1.5°). The actual efficiency was measured by the manufacturer on a test piece made at the same time as the grating and agrees well with the calculated efficiency [22].

Table 3
Parameters for the blazed VLS plane gratings.

Grating parameters		
Ruled Area (mm × mm)	170 × 25	161 × 26
Blaze angle (degrees)	0.312 +/−0.02	0.9 +/−0.07
Anti Blaze angle (degrees)	4.57 +/−0.64	4.6
Roughness (nm rms)	0.42	0.11
VLS parameters:		
a_0 (l/mm)	300.02 +/−0.02	900
a_1 (l/mm^2)	−0.0268 +/−0.00004	−0.080190 +/−0.0000329
a_2 (l/mm^3)	$+1.83 \times 10^{-6}$ $+/-1.3 \times 10^{-6}$	$+5.877 \times 10^{-6}$ $+/-0.58 \times 10^{-6}$
Pt coating (nm)	28 +/−2	29

The peak efficiency for the 300 l/mm (900 l/mm) grating reaches over 40% (20%) and is larger than 10% (7.5%) over the whole working energy range. Since the monochromator is in focus for fixed included angles over a wide range of grating angles the energy can be changed over a broad energy range without changing the included angle. By changing the included angle the peak efficiency can be moved to higher or lower photon energies. The efficiency over the 600–1900 eV photon energy range is greater than 28% for the 300 l/mm grating and 15% for the 900 l/mm grating. The resolving power of 5000 can also be achieved at for the different included angles up to 1300 eV with 30/50 μm (entrance/exit) slits and up to 1600 eV with 30/25 μm (entrance/exit) slits for the 300 l/mm grating. The 5000 resolving power is easily achieved at all energies for the 900 l/mm grating with 30/50 μm (entrance/exit) slits.

5.2.2. Deflecting mirror

The cylindrical deflecting mirror (DFM) fabricated by SESO, sagittally focuses the virtual source point produced by the grating at the exit slit. An additional function of the cylindrical mirror is to deflect the beam towards the XMCD branch of the beamline in order to separate it from the RIXS branch. When the RIXS branch of the beamline is used, the cylindrical mirror is totally removed by a 10 mm horizontal translation perpendicular to the beam. The cylindrical mirror is mounted on a hexapod support which gives 6 degrees of freedom [12] and there is an internal fine adjustment of the horizontal angle (rotation about z) using an in-vacuum piezoelectric actuator with capacitive sensor (PI). The pressure in the vacuum chamber is $< 2 \times 10^{-9}$ mbar.

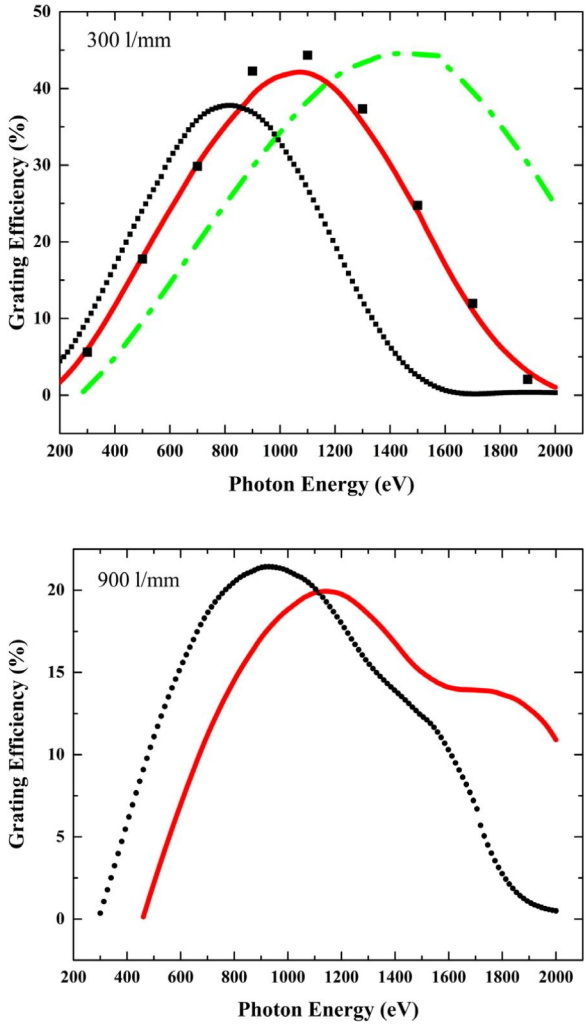

Fig. 5. Upper panel: The calculated grating efficiency of the 300 l/mm Pt coated VLS blazed grating with total included angles 175° (small black dots), 176° (red solid line) and 177° (green dot-dashed line). The measured efficiency points are shown as large squares [22]. Lower panel: The calculated grating efficiency of the 900 l/mm Pt coated VLS blazed grating with total included angles 175° (black dots), 176° (red solid line).

5.2.3. XMCD exit slit

The exit slit was also fabricated by TOYAMA and is identical to the entrance slit minus the unneeded water cooling. It is situated at ~36 m after the grating (~101 m from the source) and is typically set to a vertical aperture between 5 μm and 50 μm. A ± 300 mm travel along the beam direction is used to establish the best focal condition but once determined the slit is fixed in position. The exit slit can also be scanned in the vertical direction and rotated around the beam axis.

5.2.4. XMCD refocusing optics

The refocusing optics are situated approx. 16 m after the exit slit. The first mirror is an elliptically bent cylindrical mirror (HRM) deflecting the beam horizontally. The collimated beam produced by the M2 mirror can be focused at the sample position for either end-station, 1 or 2 (see Fig. 1), or a defocused beam can be produced when sample damage is an issue. The mirror is mounted on a hexapod support [12] and has an in-vacuum piezoelectric activator and capacitive sensor (PI) to allow a fine adjustment of the beam in the horizontal plane (rotation about z). The horizontal mirror is followed by a vertically refocusing elliptically bent cylindrical mirror (VRM) in a Kirkpatrick–Baez (KB) configuration. Both the horizontal and vertical mirrors were fabricated by Coastline Optics and ESRF designed benders were used [23]. The vertically bent mirror

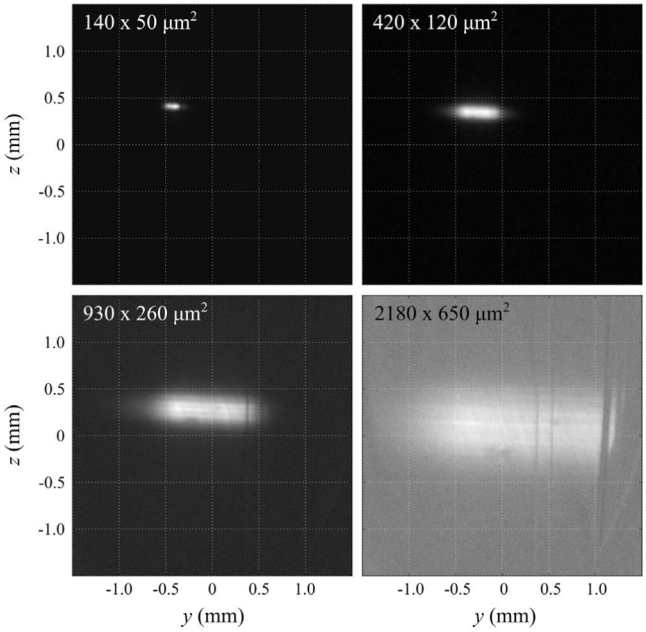

Fig. 6. The beam size can be adjusted in both directions by using two mirror benders. The horizontal × vertical spot size is indicated on each panel.

images the monochromator exit slit at the sample position (1 or 2, see Fig. 2) or can be used to defocus the beam. At the sample position 1, where the high field superconducting magnet is positioned, a beam size from ~100 μm ×10 μm (H ×V) to ~2000 μm ×800 μm can be produced. Fig. 6 shows the measured beam size in different configurations using a beam viewer as described in Section 10. The beam can be focused separately in the horizontal or vertical plane as also shown in Fig. 6. In order to keep the beam in the horizontal plane the final mirror is a plane mirror (RPM). The plane mirror is mounted in a +/− configuration with the vertical refocusing mirror on a common hexapod support. An in-vacuum piezoelectric activator with capacitive sensor (PI) is used on the final mirror for fine adjustment of the beam at the sample position in the vertical plane. The pressure in the mirror chambers is $< 2 \times 10^{-9}$ mbar. The last two mirrors have B_4C and Platinum strips for harmonic rejection and they are selected by a horizontal translation using the hexapod.

5.3. XMCD performance

5.3.1. XMCD resolving power

The XMCD branch was designed to have a resolving power of better than 5000 up to 1 keV with a 50 μm exit slit and also at higher photon energies by closing the exit slit with the high flux 300 l/mm grating. Better resolution can be achieved using the 900 l/mm grating. A standard way of checking the resolving power is to measure the absorption spectra from nitrogen and neon gas. The natural line width is relatively well known (see for example: Prince et al. and references therein [24]) and so the contribution from the beamline can be determined when it is comparable or larger than the natural line width. Fig. 7 shows the nitrogen and neon gas absorption spectra measured with the beamline gas cell (see Section 10) using the 300 l/mm grating. The monochromator entrance and exit slit openings were 30 μm and 50 μm respectively. The measured width of the lowest energy peak is 130 meV and 311 meV for the nitrogen and neon edges respectively. This gives a de-convoluted Gaussian width of 32 meV (137 meV) corresponding to a resolving power ($\Delta E/E$) of >12 000 (6000) at the nitrogen (neon) edge. These resolving power values are comparable to those obtained from a full ray tracing including all slope errors using SHADOW [25]. Fig. 8 shows the measured resolving power at the neon edge as a function of the exit slit size. At small slit sizes > 7000 resolving

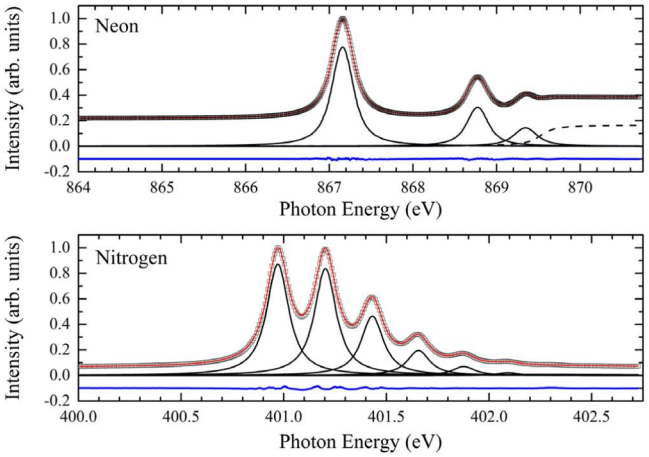

Fig. 7. Gas phase absorption spectra for nitrogen (lower) and neon (upper) with the corresponding fits. The experimental data are shown as open squares, the individual fitted peaks as solid black lines and the overall fit including background as a solid red line through the data points. The residue is shown below the fits.

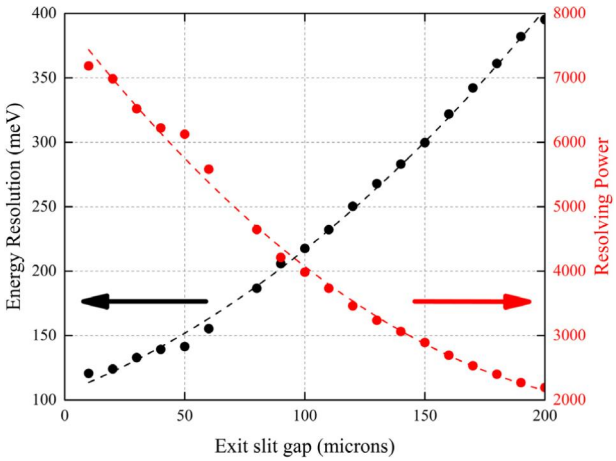

Fig. 8. Energy resolution (left) and resolving power (right), as a function of the monochromator exit slit size, as determined from the Ne K-edge (867.1 eV) measurements. The monochromator entrance slit was set to 30 μm.

power can be achieved. For XAS experiments this resolution is sufficient as the core-hole lifetime dictates the spectral line widths.

5.3.2. *XMCD photon flux*

The photon flux has been measured just before the sample using a AXUV100 silicon diode (IRD photodiode, Opto Diode Corp.) (see Section 10). The upper panel of Fig. 9 shows the measured flux with three different fixed plane mirror angles, fixed entrance and exit slit sizes (30 and 50 μm slits respectively) using only the 2.5 m undulator. The calculated flux is shown as a black dashed line in Fig. 9 with a pre-mirror angle of 2 degrees. The source was calculated using SRW [26] for a 2.5m undulator at the centre of the straight section. The transmission of the beamline was calculated using SHADOW [25] including the slope errors of the optics. The reflectivity of the optical elements were calculated using the CXRO reflectivity tool [27]. The grating efficiency was calculated using REFLEC [21]. The flux is normalised to a ring current of 100 mA. The measured flux was found to be lower by a factor of ~1.6 at the reference energy of 930 eV. The lower panel of Fig. 9 also shows the flux for the 900 l/mm grating for the same slit sizes which corresponds to approx. a factor of 3 better energy resolution. The flux scales by what would be expected given the better bandpass and the lower efficiency of the higher density grating.

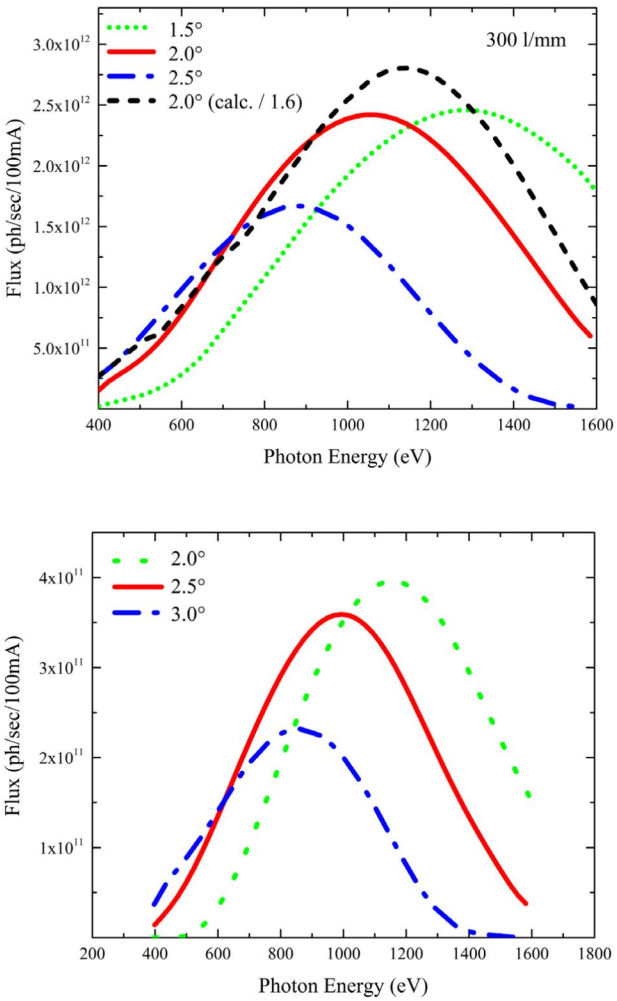

Fig. 9. Upper panel: Measured flux (circular polarised) with different pre-mirror angles (dot-dashed blue line, 2.5°; red full line, 2°; dotted green line, 1.5°) for 30/50 μm entrance/exit slits and the 300 l/mm grating. The experimental data at 2° is compared with the calculated flux (black dashed line) reduced by a factor of 1.6 – see text. Lower panel: Measured flux (circular polarised) with different pre-mirror angles (blue dot-dashed line, 3°; red full line, 2.5°; green dotted line, 2°) for 30/50 μm entrance/exit slits and the 900 l/mm grating.

6. XMCD branch end stations

The XMCD branch of the beamline serves two experimental areas (1 and 2), see Fig. 1. The first is the XMCD end station with a superconducting 9 T high field magnet. This end station has been described elsewhere [28]. The second experimental area is in-line with the first i.e. the beam passes through the high field magnet to the other station. This station is an "open" experimental area for User chambers or special experimental set-ups. Recent experiments in this area have used an in-house end station for time-resolved magnetic holography measurements [29]. The room is approx. 5 ×5 m^2 and since the mirror benders allow for focusing (horizontally and vertically) at any distance in the room there is a lot of flexibility for installing instruments. The room has its own control room for preparing experiments independently of the other two experimental areas. The XMCD and RIXS end stations also have their own independent control rooms – see Fig. 1. This allows for efficient use of the beamtime.

7. RIXS branch

7.1. *RIXS optical concept*

In order to achieve the very high energy resolution the beamline monochromator uses an optical concept based on a focusing variable

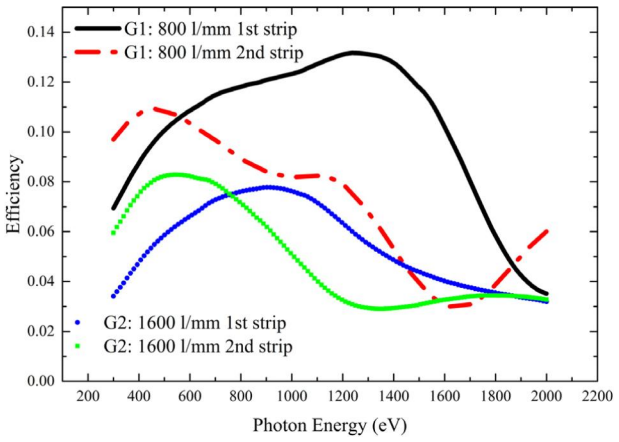

Fig. 10. Calculations of the grating efficiency: black line G1(800 l/mm)1st strip; red dashed line G1(800 l/mm) 2nd strip; blue circles G2 (1600 l/mm) 1st strip; green squares G2 (1600 l/mm) 2nd strip (see Table 4).

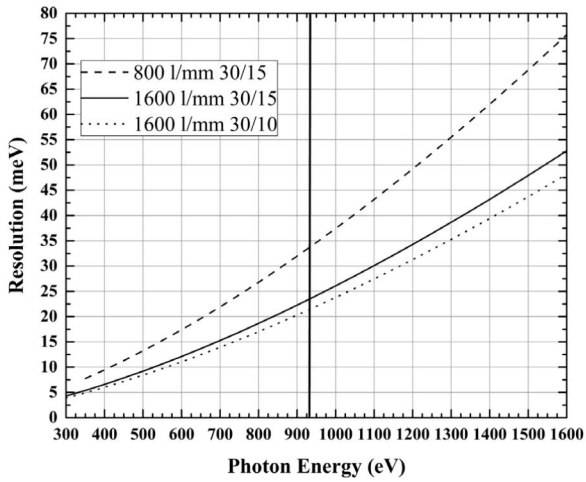

Fig. 11. Beamline energy resolution expected for the 800 l/mm and 1600 l/mm gratings with different monochromator slit settings (entrance/exit slit sizes). The vertical line is at the reference photon energy for the copper L_3 edge at ~930 eV.

line spacing (VLS) plane grating monochromator (PGM) [30–35]. There is just a plane mirror and VLS plane grating between the source (entrance slit) and exit slit. This differs from the XMCD branch that has a focussing mirror after the grating which additionally contributes to the energy resolution.

The angle of incidence on the mirror is given by

$$\gamma = \frac{\alpha - \beta}{2} - \delta$$

Where β is the diffraction angle (negative) and α is the angle of incidence (positive). If $\delta = 0$ the input and output beams are parallel and, as in our case, in the horizontal plane. By choosing other values for δ the monochromator efficiency can be improved but the beam is no longer in the horizontal. Given the very long exit arm of the monochromator even a small angle would put the beam at an unacceptable height so we choose to keep the beam in the horizontal plane.

The VLS grating line density is given by:

$$D(w) = a_0 + a_1 w + a_2 w^2 + a_3 w^3 \ldots\ldots$$

Where $D(w)$ is the line density (l/mm) along the beam direction, $w = 0$ is the centre of the grating with line density a_0, and the positive direction is towards the exit slit.

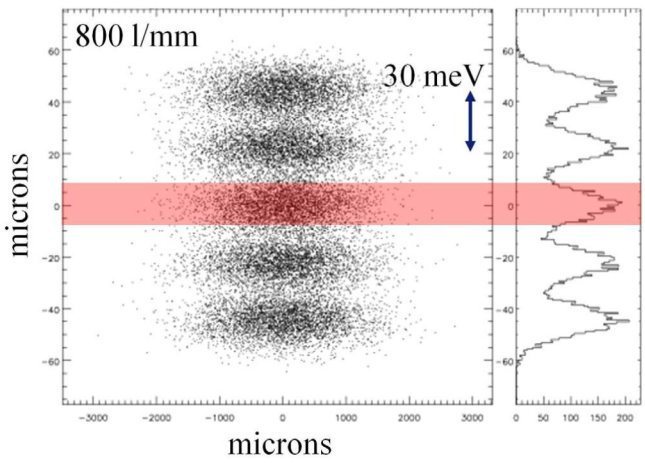

Fig. 12. SHADOW ray tracing for 5 beams centred at hν = 1000 eV separated by 30 meV for the 800 l/mm grating. The red shaded area gives the acceptance of a 15 μm exit slit. (For interpretation of the references to colour in this figure legend, the reader is referred to the web version of this article.)

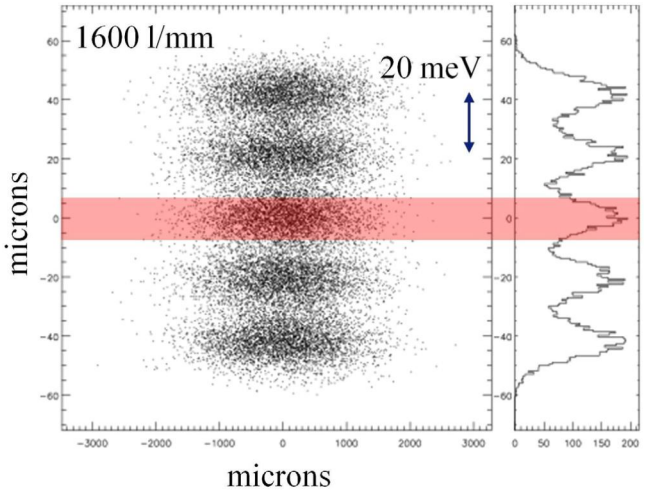

Fig. 13. SHADOW ray tracing for 5 beams centred at hν = 1000 eV separated by 20 meV for the 1600 l/mm grating. The red shaded area gives the acceptance of a 15 μm exit slit. (For interpretation of the references to colour in this figure legend, the reader is referred to the web version of this article.)

The linear coefficient a_1 can be chosen to zero the defocus term at a particular energy [33]:

$$a_1 = \frac{\left(\frac{\cos^2\alpha}{r_1} + \frac{\cos^2\beta}{r_2}\right)}{n\lambda} :$$

where r_1 is the entrance arm length (in our case the entrance slit to grating distance), r_2 is the grating to exit slit distance, n is the diffraction order ($n = 1$) and λ is the wavelength [31]. If the monochromator is operated with a fixed C_{ff}, where $C_{ff} = \cos\beta/\cos\alpha$ then the defocus can be essentially zeroed at all energies and if needed, a very slightly different C_{ff} at each energy can be used. In our case $C_{ff} =\sim 3.1$ for both the 800 l/mm and 1600 l/mm gratings. The final values found during commissioning were 3.11 and 3.15 respectively. This allows us to achieve the required resolving power and cover the energy range with a reasonable grating efficiency.

Likewise the a_2 terms can be chosen to zero the coma [33]:

$$a_2 = \frac{3\left(\frac{\sin\alpha\cos^2\alpha}{r_1^2} + \frac{\sin\beta\cos^2\beta}{r_2^2}\right)}{2n\lambda}$$

Table 4
RIXS branch grating parameters.

Grating parameters	G1 1st strip	G1 2nd strip	G2 1st strip	G2 2nd strip
Groove density	800	800	1600	1600
Ruled Area (mm × mm)	180 × 12.5	180 × 12.5	180 × 12.5	180 × 12.5
c/a	0.61	0.63	0.67	0.69
Groove depth (nm)	9.52	13.26	5.7	8.45
Roughness (nm rms)	<0.15	<0.15	<0.15	<0.15
Au coating thickness (nm)	50	50	50	50
VLS parameters:				
a_0 (l/mm)	799.878	799.878	1599.746	1599.746
a_1 (l/mm^2)	0.058775	0.058775	0.11789	0.11789
a_2 (l/mm^3)	1.811×10^{-6}	1.811×10^{-6}	2.9944×10^{-6}	2.9944×10^{-6}

Although only strictly valid at a single energy the variation over the 400–1600 eV energy range is ~0.4% and the contribution to the overall energy resolution is small compared to other contributions. The tolerances for the VLS parameters were determined by ray tracing using SHADOW [25]. The nominal values for the 800 l/mm grating were:

$a_0 = 800$ l/mm, $a_1 = 0.0592$ l/mm^2 and $a_2 = 1.62 \times 10^{-6}$ l/mm^3.

For the 1600 l/mm grating:

$a_0 = 1600$ l/mm, $a_1 = 0.11831$ l/mm^2 and $a_2 = 3.2426 \times 10^{-6}$ l/mm^3.

For continuous energy scans the mirror and grating are scanned together. Otherwise they are moved together in a step-by-step manner. The undulator gap is typically scanned with the monochromator.

7.2. RIXS components

7.2.1. RIXS grating parameters

The RIXS branch gratings were made by Shimadzu. The final measured parameters are shown in Table 4. Two different strips with different groove depths and c/a ratios were fabricated for both the 800 l/mm and 1600 l/mm gratings. The idea was to optimise the efficiency at different photon energies. Using the values for the 800 l/mm grating in the table gives higher efficiency in the 300–500 eV energy range for the 13.26 nm depth grating and higher efficiency above 500 eV for the other 800 l/mm grating strip. For the 1600 l/mm grating the 8.45 nm grove depth grating is more efficient in the 300–800 eV range and the 5.7 nm groove depth grating for 800 eV and above. The relative efficiencies for the 800 and 1600 l/mm gratings are shown in Fig. 10. The 1600 l/mm grating is approx. 40% less efficient than the 800 l/mm grating at 1000 eV photon energy.

The peak efficiency reaches over 12% (8%) for the 800 l/mm (1600 l/mm) grating. The grating efficiencies were calculated using REFLEC [21].

7.2.2. RIXS exit slit

The RIXS exit slit is identical to the XMCD exit slit, see Section 5.2.3.

7.2.3. RIXS refocusing optics

The refocusing optics are situated approx. 8.8 m after the exit slit. The first mirror is an elliptically bent cylindrical mirror (VRM) deflecting the beam vertically upwards. Since the vertical spot size is used as a source for the RIXS spectrometer a small Gaussian shaped beam is required. The bender can produce a 3–4 μm FWHM spot at the sample. The beam size is characterised using a razor blade mounted on the sample goniometer. Baffle slits before the mirror allow selected regions of the mirror to be illuminated aiding the characterisation of the mirror and optimising the bender. With proper adjustment a 3 μm FWHM Gaussian beam has been produced. The mirror was fabricated by Coastline Optics and an ESRF designed bender was used [23]. A second downward facing mirror deflecting in the vertical brings the beam back in to the horizontal plane. This mirror, manufactured by Zeiss, is cylindrical (HRM) and sagittally focuses the collimated beam produced by the double mirror device in the horizontal direction. The horizontal beam focus is of the order of <60 μm in size depending on the undulator settings. The mirrors are mounted on a common hexapod support. An in-vacuum piezoelectric actuator with capacitive sensor (PI) is used on the final mirror for fine adjustment of the beam at the sample position in the vertical plane. The mirrors are platinum coated with a combined reflectivity of ~60% over the entire photon energy range. The final mirror is electrically isolated so that the drain current can be used and the mirror used as an intensity monitor. The pressure in the mirror chamber is $<2 \times 10^{-9}$ mbar.

7.3. RIXS performance

7.3.1. RIXS resolving power

The objective for the RIXS branch was to achieve a combined (beamline + spectrometer) resolving power of ~30 000 at the copper L_3 edge ($h\nu$ ~930 eV). If equal contributions come from the beamline and spectrometer then each should reach a resolving power of ~42 000. For high flux operation a combined resolving power of ~17 000 was aimed at, meaning the beamline should have a resolving power of 24 000. At the copper L_3 edge this gives ~22 meV and ~40 meV for the beamline and spectrometer at the two settings, respectively. The expected beamline energy resolution with typical monochromator slit sizes is shown in Fig. 11. These are analytical calculations including the mirror and grating slope errors and the entrance and exit slit contributions with $C_{ff} = 3.1$. The ~40 meV from the beamline can be comfortably achievable with the 800 l/mm grating and 30 (15) μm entrance (exit) slits. To achieve ~22 meV energy resolution requires the 1600 l/mm grating and 30 (10) μm entrance (exit) slits. Due to the lower efficiency of the higher line density grating and the narrower band pass, this also results in a loss of intensity by a factor of four without including the spectrometer.

The expected resolution of the beamline has been checked by ray tracing using SHADOW [25]. The ray tracing included all the slope errors of the optics. An estimation of the resolution can be obtained by considering several equally energetically spaced X-ray beams and projecting them on to the exit slit plane. The beams are spaced by 30 meV and 20 meV for the 800 l/mm (Fig. 12) and 1600 l/mm (Fig. 13) cases respectively. The coloured boxes represent a 15 μm slit and show that in the 1600 l/mm case the lines are well separated with some overlap in the 800 l/mm case. Both analytical calculations and ray tracing show that it is feasible to achieve the required resolution if the slope errors of the optics are maintained. Degrading the pre-mirror and grating slope errors by 1.5 (2.0) would degrade the energy resolution by 1.25 (1.5) giving ~50–60 meV from the beamline. The beamline resolution was initially tested using gas phase measurements as described for the XMCD branch in Section 5.3.1. This allowed an optimisation of the exit slit position and the C_{ff} parameter. However, since the gas phase natural line widths are much broader than the expected resolution it is not a reliable way to determine the exact beamline resolution. Some initial tests using the Fermi level cut off measured from a gold sample using photoelectron spectroscopy indicated that the achieved resolution was as expected. However, the final optimisation was done with the RIXS spectrometer since it is the combined energy resolution that matters. As will be shown

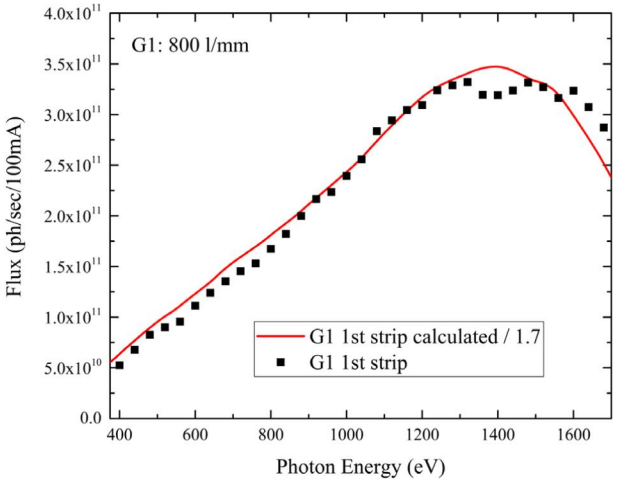

Fig. 14. Calculated (red line) and measured flux (squares) using the 800 l/mm grating (G1 1st strip, Table 4). The entrance and exit slits were 30 and 15 μm respectively. The calculated flux is reduced by a factor of 1.7 for the comparison (see text).

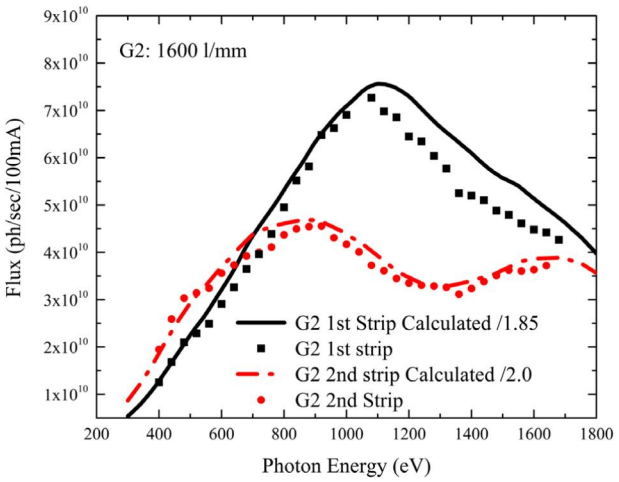

Fig. 15. Calculated (black line and red dot-dashed line) and measured flux (black squares and red dots) for the 1600 l/mm grating for strips G1 and G2 respectively (Table 4). The entrance and exit slits were 30 and 15 μm respectively. The calculated flux is reduced by a factor of 1.8 and 2 for the two strips – see text.

below, these results show that the beamline must be reaching its target resolution since the combined resolving power is achieved.

7.3.2. *RIXS flux*

The photon flux has been measured just after the sample position using a AXUV100 silicon diode (IRD photodiode, Opto Diode Corp.) (see Section 9). Figs. 14 and 15 shows the measured and calculated flux with fixed entrance and exit slit sizes (30 and 15 μm slits respectively) and the 800 l/mm (1600 l/mm) grating. For the 1600 l/mm grating data is shown for the two different strips. The flux was calculated using the same codes as described in Section 5.3.2. The measured flux was found to differ by a factor of 1.7 at the reference energy of 930 eV for the 800 l/mm grating, this is similar to the XMCD branch. The 1600 l/mm grating seems to be less efficient and the flux is lower than expected by a factor of 1.8–2 at the reference energy of 930 eV.

8. RIXS branch end station

8.1. *RIXS sample chamber*

The RIXS end station is comprised of a 711 mm diameter UHV vacuum chamber (Fig. 16) which houses a four-circle UHV diffractometer

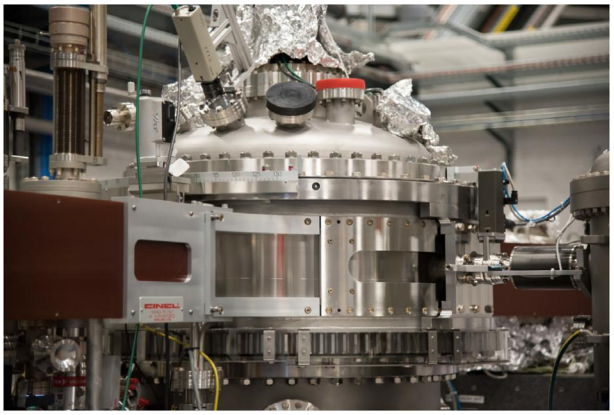

Fig. 16. RIXS sample chamber showing the differentially pumped ribbon section (centre of the picture) and the edge welded bellows connecting the chamber to the scattering arm (right) (Credit: C. Argoud/ESRF).

manufactured by HUBER. The base pressure is ~1 $\times 10^{-9}$ mbar and is pumped with two 400 l/sec ion pumps and a 700 l/sec turbomolecular pump. A sample storage chamber and fast load lock allow samples to be transferred from air into UHV without breaking the vacuum in the main chamber in approx. 30 min. The chamber and the sliding seal (see below) were manufactured by CINEL.

8.2. *RIXS diffractometer*

The RIXS diffractometer was fabricated by HUBER (Fig. 17). It is intended for a horizontal scattering geometry where the scattering plane is defined by the incoming and out-going X-ray beam and designed as a full in-vacuum four-circle diffractometer. A vertical θ (theta) ($-20°$ + $185°$) axis supports a $\pm 45°$ χ (chi) cradle which in turns supports a full 360° sample rotation ϕ (phi). The detector stage 2θ axis (two theta) ($-10°$ $+175°$) coincides with the θ axis but is fully independent from it. The sample can be moved with respect to the centre of rotation through two translations T_x (± 12 mm) and T_z (± 12 mm) located above the ϕ stage, while the sample surface can be brought to the centre of rotation using a translation T_y (± 6 mm) parallel to the ϕ axis (within 15 μrad) and located below the ϕ stage.

The total sphere of confusion was measured to be 44 μm. The axes are all orthogonal within 100 μrad. All rotations display at least 0.001° resolution and repeatability within 0.005° while the translations provide resolution within 1 μm and below for T_y with a 1:10 reduction gear, and repeatability within 2 μm.

Three photodiodes (IRD AXUV 100G 10 × 10 mm^2) are mounted on the detector arm. One diode is fully open and is used for initial peak search and alignment. The current is read and converted through a FEMTO DLPCA-200 current amplifier. The acceptance of the second (third) diode is reduced by a 2 (1) mm diameter to decrease the scattered background seen by the detector and increase the angular resolution in Resonant Elastic X-ray Scattering (REXS) experiments. The current is read and converted through a KEITHLEY 428 electrometer.

The mounting base to centre height is 50 mm ± 6 mm depending on T_y. This allows various sample setups to be installed. In a standard configuration, the sample stage is fitted with a liquid helium cooled shuttle receptacle fully compatible with an in-vacuum sample transfer via a load-lock and a sample storage chamber kept in UHV conditions (in the 5 $\times 10^{-9}$ mbar base pressure). The shuttle receptacle (Fig. 18) is cooled by a liquid Helium flow cryostat (CryoVac) through copper braids that preserve the degrees of freedom of the sample. Due to the copper braid and electrical connections ϕ is restricted to a $-45°$ $+135°$ range, while χ and θ are preserved over their full working range. The receptacle is thermally decoupled from the mounting base by a specially designed cone manufactured initially in Torlon PAI (polyamide-imide) and finally

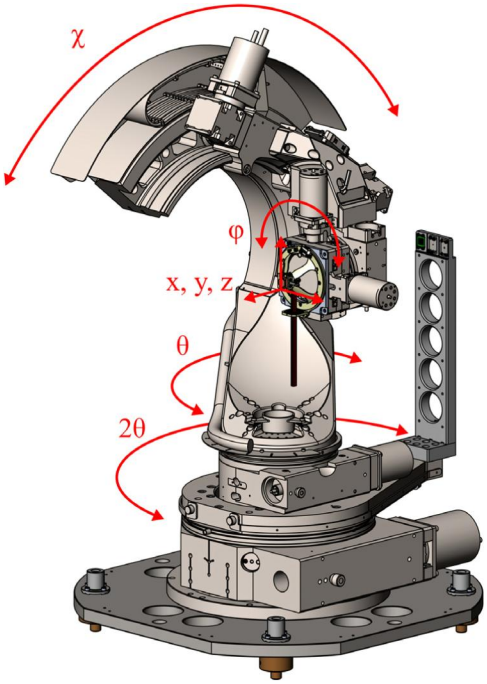

Fig. 17. The in-vacuum sample goniometer showing the various motions.

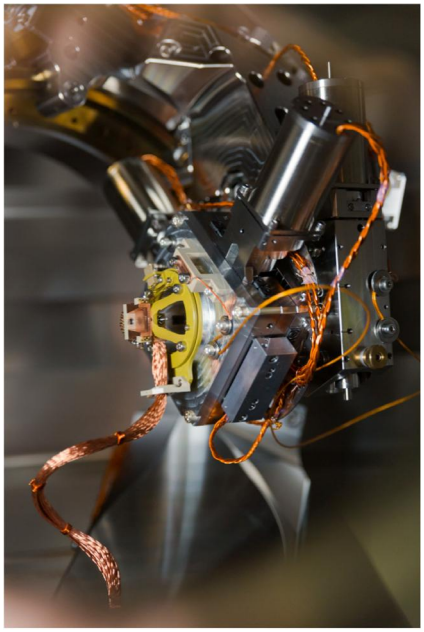

Fig. 18. The RIXS sample shuttle receptacle showing the sample mounting position and the cooling braids. (Credit: P. Jayet/ESRF).

in PEEK (Polyether ether ketone). The minimum achievable sample temperature in these conditions is 15 K at a liquid helium consumption rate of about 0.17 l/min. Normal low temperature operation is 20 K with a much lower liquid helium consumption of ~1 l/hour.

Electrical connections to the sample are available (8 contacts) and the sample plate is electrically insulated from the receptacle. As a standard, the drain current of the sample is fed into a KEITHLEY 428 electrometer. Additional contacts can be used to measure the temperature of the sample plate, perform transport measurements and/or apply electric fields.

8.3. *RIXS spectrometer*

High resolution RIXS spectroscopy is still a young technique, so a new instrument aiming at exploring its full potential must be designed to combine cutting edge performance with ample flexibility and ease of use. The goal was thus to achieve an improvement of a factor 2 to 3 in combined resolving power with respect to the best performing facility in 2012, while keeping a similar count rate. The aim was also to allow for the first time the continuous variation of the scattering angle over 100°, a diffractometer-class sample manipulation (Section 8.2), and the measurement of the polarisation resolved high resolution spectra. The special measurement UHV chamber for the continuous rotation of the spectrometer and the sample environment have been described above and in this section we will present the optical scheme of the spectrometer and polarimeter.

The key for improving the resolution with respect to the SAXES instrument [5,6] at the ADRESS beam line [36] of the SLS/PSI is the doubling of the total length of the spectrometer, from sample to detector. For the same vertical spot size on the sample (source for the spectrometer), grating line density and detector spatial resolution, and neglecting the slope error contributions, the bandwidth of the spectrometer is proportional to the inverse of the total length. To fully exploit this gain the resolution of the beam line monochromator must be tuned to the spectrometer resolution and here again a longer device can achieve this without sacrificing efficiency. Therefore the unprecedented space available (Fig. 1) at the ESRF for long beam lines was exploited and the end-station and the new spectrometer (ERIXS) were designed using a 12 m maximum length boundary condition. The experience accumulated with SAXES indicated that a physical entrance slit is not needed anymore, thanks to the high stability of the incident beam position and beam size at the sample. Also the reliability, stability and ease of tuning of SAXES meant that the optical and mechanical scheme could be mostly replicated. To keep the count rate per experimental point unchanged the reduction of the bandwidth needed to be compensated by an increase in detection efficiency, which was obtained by adding a parabolic mirror collecting a larger angle in the horizontal direction (the vertical acceptance is comparable) and by increasing the grating reflectivity in diffraction, thanks to a smaller groove density. The lower dispersion is then compensated by a smaller source and a higher detector resolution.

The polarisation analysis has been included since the beginning of the design of ERIXS, taking advantage of the prototype [37] installed on the AXES spectrometer [38,39] at ID08 of the ESRF (operational until 2013). That device had demonstrated that a reliable measurement of the linear polarisation of the scattered radiation could be obtained at the cost of approximately a factor 10 in intensity while preserving the energy resolution. Moreover, the collimation of the beam by the parabolic mirror in the spectrometer allowed the implementation of an original way [37] of widening the energy window where the polarimeter provides a flat response, thus covering several eV of the measured RIXS spectra. This property is a key for making the polarimeter sufficiently user-friendly to be open for public access.

8.3.1. *RIXS spectrometer components*

The spectrometer arm is composed of three vacuum chambers (Fig. 19). All the spectrometer vacuum chambers are pumped with ion pumps and are at $<2\times10^{-9}$ mbar base pressure.

The first two are supported on a granite base that is also an air pad. The first chamber, at 1.1 m, contains a collimating parabolic mirror scattering in the horizontal direction with a 2° incidence angle.

The second chamber contains two VLS spherical gratings scattering in the vertical direction. This chamber can be moved on slides along the scattering arm to change the sample to grating distance (2.5 m +/− 0.4 m). The gratings are mounted on Micos in-vacuum goniometers allowing for independent angular motions (2° +/− 5°) and common horizontal

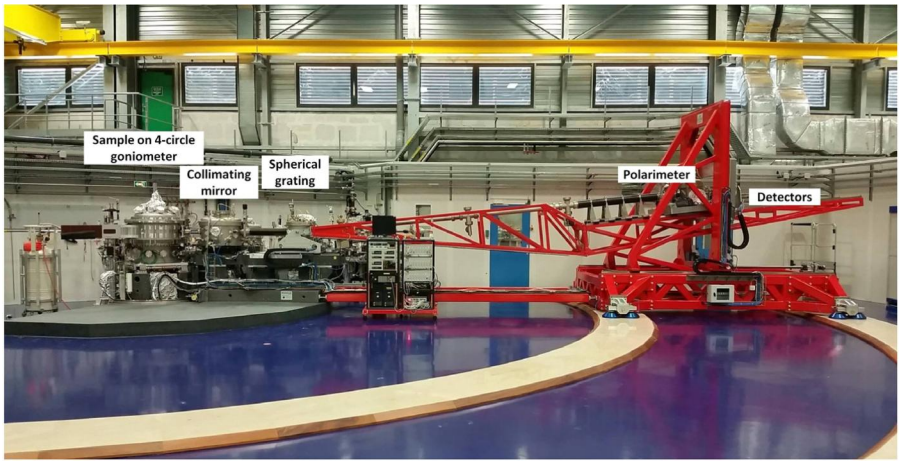

Fig. 19. Side view of the ERIXS spectrometer.

(perpendicular to the beam) (+/− 77.5 mm) and vertical motions (+/− 6.5 mm).

The third chamber is mounted at the end of the scattering arm steel structure which allows the detector to be positioned in the direction along the scattering arm (11 m +/− 1 m) and in the vertical direction (1.050 m +/− 0.7 m). This chamber contains the multilayers for polarimetric analysis of the scattered beam. The position of the multilayers can be adjusted with in-vacuum Micos mechanics. The multilayers can be moved vertically (+/− 75 mm) to select the correct part of the multilayer for the scattered energy. The multilayer can be rotated about the vertical axis (−30°–+95°) to find the correct scattering angle and moved in and out of the direct beam for detection with or without the analyser (26 mm). There is also a χ motion that allows the scattering angle to be adjusted (+/− 5°).

At the end of the chamber there are two Andor Ikon L soft X-ray direct illumination CCD detectors one for the direct beam and one for the beam diffracted by the multilayer. The latter is mounted on external mechanics with bellows to allow the distance between the multilayer and the CCD to be adjusted so that the two CCD cameras can be at the same distance from the sample (+/− 20 mm). The angle can also be adjusted to set the correct scattering angle (40° +/− 10°).

The steel structure is mounted on 8 airpads (IBS D300). When an air pressure of 5 bar is applied to these air pads and the granite airpad structure the entire scattering arm rises approx. 70 μm. The structure is guided by a circular rail mounted close to the sample chamber and a small stepper motor mounted at the end of the steel structure moves the arm over the 100° range. Once in position the air pressure is cut and the scattering arm is fixed in position. The granite airpad moves on a very flat (10 μrad planarity with Δz = 40–50 μm @ 10 m) granite floor (Microplan) and the airpads move over circular marble tiles which have been polished (70 μrad planarity, Δz = 300–400 μm @ 10 m). The arm moves at approx. 4–5 s/degree. The angle is measured using an encoder (Mercury II MII 1610S-20) on the guide rail. By moving the ribbon containing the vacuum port on the sample vacuum chamber (see Fig. 16) in unison with the scattering arm (using the encoder), the scattering angle can be changed continuously from 150° to 50° degrees (0° is forward scattering). The vacuum pressure rises to the low 10^{-8} mbar range in the RIXS sample chamber when a motion occurs but recovers quickly once the motion has finished.

8.3.2. *RIXS spectrometer optics*

The spectrometer optical layout is based on a spherical grating with variable line spacing (VLS), working at the first internal diffraction order. The optical design followed the procedure described in Ref. [4] with the corrections added by V. Strocov [5], where the total distance from sample to detector L_0, the central groove density a_0, the deflection angle $2\theta_0$, the source size S_1, the detector resolution S_2 and the

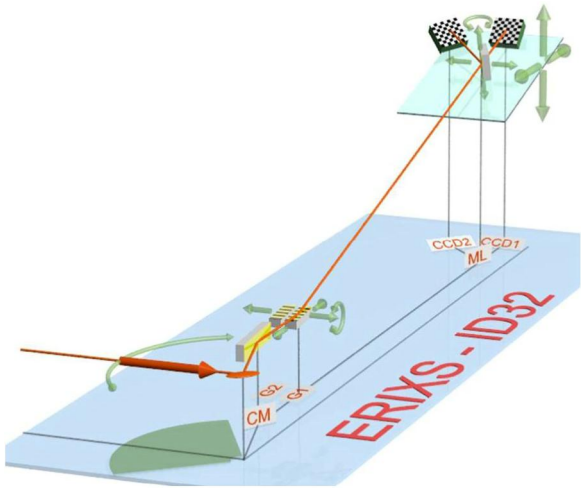

Fig. 20. The simple optical lay-out of ERIXS is composed of a horizontally collimating mirror (CM) and two interchangeable VLS spherical gratings (G1 and G2) with different groove density. The detector (CCD1) is at 25 degrees from the incident photon direction. Optionally a multilayer mirror can be inserted to deflect the beam by approximately 40 degrees perpendicularly to the dispersion direction: the spectrum recorded on CCD2 is different from the direct one due to the dependence of the reflectivity on the polarisation of the photons. The main mechanical degrees of freedom needed to optimise the resolution at different photon energies are shown by the green arrows.

incidence angle on the detector γ, all at the reference photon energy E_0, determine the linear a_1 and quadratic a_2 terms of the VLS polynomial density law and radius of curvature R, in a way that optimises the balance among different contributions to the band width. Two gratings were optimised for a resolving power $E/\Delta E$ around 25 000 and 40 000 at E_0 for optimum flux (grating G2) or highest resolution respectively (grating G1). The parameters are summarised in Table 5. The total space in the experimental room allows $L \leq 12$ m, and this space has been fully exploited. Such a long distance would severely limit the horizontal angular acceptance when using standard CCD detectors of 25 mm lateral size. Consequently, a 600 mm long parabolic-cylindrical mirror at 1.1 m from the sample has been inserted which collects ~20 mrad at ~88° incidence angle producing a 20 mm wide horizontally collimated beam down to the detector. By considering an average reflectivity of 0.6 for the mirror the horizontal acceptance is thus 7 times larger than in the SAXES instrument [5] operated with a 25 mm detector.

The overall optical and mechanical scheme is shown in Fig. 20, together with the main adjustments available to optimise the resolution at different photon energies.

Table 5
The design parameters of the two spectrometer gratings, and expected performances from analytical calculations and numerical simulations with REFLEC [21] and SHADOW [25].

Spectrometer parameters	Symbol	G1	G2
Energy range (eV)		400–1500	400–1000
Reference energy (eV)	E_0	900	800
Total lengths at reference energy (mm)	L_0	10 700	10 800
Groove density (l/mm)	a_0	2500	1400
VLS linear term (l/mm^2)	a_1	0.362	0.170
VLS quadratic term (l/mm^3)	a_2	-6.39×10^{-5}	-7.10×10^{-5}
Radius of curvature (mm)	R	122 000	122 000
Incidence angle at reference energy (degrees)	α	87.89	88.00
Half of the total included angle at reference energy (degrees)	θ	86.34	86.86
Entrance arm at reference energy (mm)	r_1	2545	2493
Slope error of grating (nrad rms)	σ	200	200
Vertical spot size on the sample = Source size in dispersion direction (μm)	S_1	3	3
Actual CCD spatial resolution (μm)	S_2	7	7
Angle of incidence on the detector, from surface (degrees)	γ	25	25
Horizontal angular acceptance with collimating mirror (mrad)		20	20
Vertical acceptance with coma correction (with 200 mm footprint) (mrad)		2.9	2.8
Resolving power at reference energy (calculated)	$E/\Delta E$	42 500	28 000
Efficiency of grating at reference energy (calculated)	ϵ_0	0.055	0.11

The in-vacuum CCD cameras are optimised for the soft X-ray range (thinned and back-illuminated). They have 2048 × 2048 square pixels (13.5 μm) and are Peltier cooled to −90 °C. The effective in-plane spatial resolution is around 7 μm, thanks to the single photon detection and centroid determination [40]. The full frame is read at a 2 MHz pixel rate in approximately 2.5 s. As in most cases the RIXS spectrum extends over only 30% to 50% of the sensor in the dispersion direction, the readout time is of the order of 1 s, meaning that exposure times down to 5 s are possible without relevant decrease of the acquisition duty cycle. In most cases the intensity on the detector is compatible with acquisition times of 30 s to 150 s without pile-up in the pixels, even in the most intense spectral regions. The measured vertical spot size ($S1$) on the sample is usually 3–4 μm, fully compliant with the design value. The gratings were designed and polished to the same radius R for convenience of production by Zeiss· the measured residual figure error over the whole surface to be grooved is 250 nrad rms. They were grooved by a lithographic method with trapezoidal profile over an area of 30×200 mm^2; G1 was made by JY HORIBA and G2 by SHIMADZU with groove depth 4.0 nm and 7.5 nm respectively, and aspect ratio c/a = 0.65 and 0.66 respectively.

Fig. 21 shows that the two gratings can cover their respective energy ranges in conditions of perfect coma aberration cancellation by fully exploiting the ranges of r_1 and the detector position (700 mm and 2000 mm respectively). Moreover the zero order can be put on focus for $\alpha \sim 88.05°$; this feature can be used to image the source onto the detector surface, thereby using the spectrometer as a microscope to check the actual size of the source.

The main characteristics of the spectrometer, in terms of energy resolution and dispersion on the detector, are presented in Fig. 22 for the two gratings. These results assume a perfect cancellation of the coma aberration, which has been checked at selected energies by ray-tracing and finally confirmed by actual measurements of high resolution RIXS spectra at the Ti, O, Mn, Fe, Co, Cu and Ce edges.

8.3.3. *RIXS spectrometer polarimeter*

The polarimeter was designed, following the concept proposed in Ref. [37], to widen the intrinsic band-pass of the multilayer mirror given by the Bragg reflection condition. To achieve this, a graded multilayer was used where the thickness of the bi-layers changes in the dispersion direction to match the energy of the X-rays dispersed by grating G2 (Table 5). In this way, with the ML mounted quite close to the detector where the energy separation is almost complete, it is possible to have the Bragg reflection condition fulfilled in a wide energy range (at least 20 eV) at the same reflection angle (see Fig. 23).

This scheme is easier to realise with a collimated beam in the horizontal direction, because in the case of a diverging beam a horizontal grading would be also necessary. By moving the ML mirror in the grading direction it is possible to cover a wide range of energies. The choice of the reflection angle (θ, measured from the surface) is dictated by a compromise between maximising the average reflectivity for the two linear components (σ and π, normal and parallel to the reflection plane respectively) and increasing the relative difference of the two values in order to maximising the statistical figure of merit: $M = S_{\text{eff}} R_{\text{ave}} = \left(\frac{R_\sigma - R_\pi}{R_\sigma + R_\pi}\right)^2 \sqrt{R_\sigma R_\pi}$.

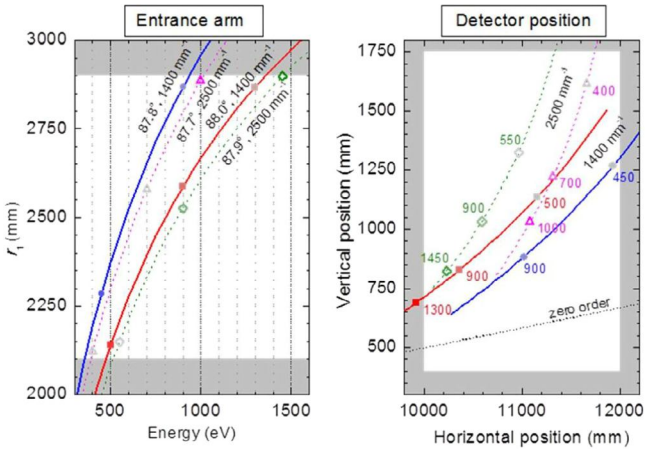

Fig. 21. The position of the gratings, namely the entrance arm r_1 and the incidence angle α, need to be adjusted to cancel the coma aberration as function of the photon energy to be analysed. The left panel shows, for both gratings, the optimal values of r-for two sensible choices of α (the grey areas are outside mechanical limits of the instrument). The panel on the right shows the detector positions for the same cases (symbol shape and colours are consistent between the two panels).

For the copper L_3 energy (~930 eV), a reference for RIXS experiments on high Tc superconducting cuprates, and using W/B_4C for the ML the theoretical optimum is obtained for $\theta \sim 20°$ where $R_\sigma \simeq 0.140$ and $R_\pi = 0.085$ [37]. At larger θ the intensity loss would be too strong: in particular at $\theta = 45°$, ideal for the polarisation selectivity because $R_\pi = 0$ and $S_{\text{eff}} = 1$ (Brewster angle) the σ reflectivity drops to 0.012, incompatible with the use of the device for real measurements. An appropriate grading allows to cover with two MLs the crucial ranges 500–560 eV (including oxygen K and V $L_{2,3}$ edges) and 670–960 eV (for Fe, Co, Ni, Cu $L_{2,3}$ and La, Ce, Pr $M_{4,5}$ edges), with a total length of 120 mm. It has to be noted that the period gradient is dictated by the energy dispersion of the grating: the polarimeter has been designed for the grating G2, and the total extension of the energy range is dictated by mirror size constraints. Fig. 24 shows the main design parameters of the double ML and the corresponding reflectivities for $\theta = 20°$. The two multilayers, obtained by coating flat Si substrates, are 80 mm wide to

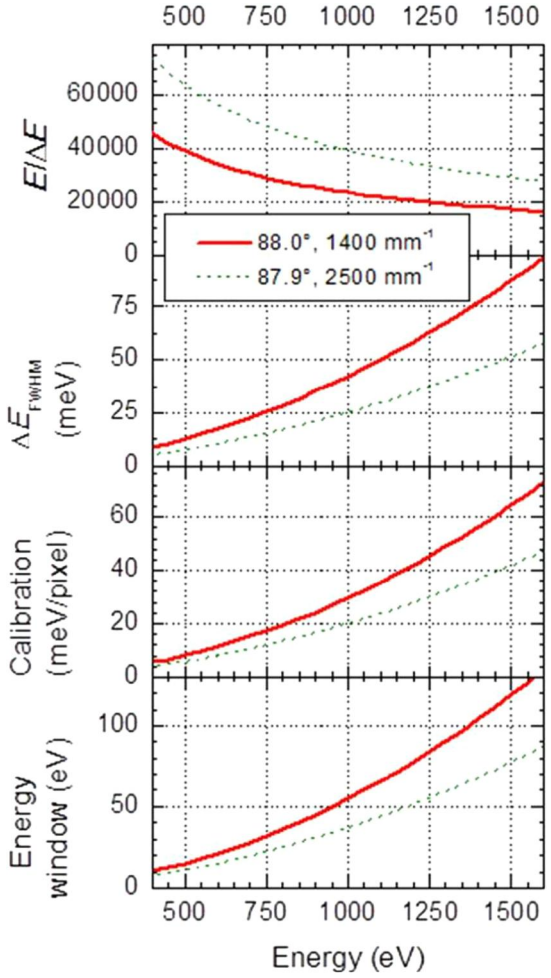

Fig. 22. The resolving power, band width, pixel to energy conversion and total energy window for the two gratings as function of the photon energy. The parameters listed in Table 5 were used for the calculation.

accept the full 22 mm wide beam at 20° incidence (65 mm footprint). The transverse position of the ML is adjustable with precision with in-vacuum translation stages, and rocking curves can be made by an in-vacuum rotation too. The design, construction and characterisation of the two ML are described elsewhere [41].

9. RIXS performance: Combined energy resolution

The ultimate aim of the RIXS project, in terms of energy resolution, is to achieve a combined resolving power of 30 000 at the copper L_3 edge (~932 eV) i.e. 31 meV. To test this, an elastically scattered beam from a carbon tape is used. The results are shown in Fig. 25. Three configurations are normally used: high flux using both low line density gratings (800 l/mm and 1400 l/mm) (Fig. 25a); medium resolution configuration, using the low line density beamline grating and the high line density spectrometer grating (i.e. 800 l/mm and 2500 l/mm) (Fig. 25b) and high resolution mode using both the high line density gratings (Fig. 25c). The monochromator entrance and exit slit sizes were 30 μm and 15 μm, respectively. The low resolution/high flux configuration gives reasonable resolution (56 meV) and intensity. The medium resolution option gives a better resolution (41 meV) with some loss of intensity and the high resolution configuration gives lower intensity but achieves the target resolution (30 meV). The resolution and flux can be additionally traded by changing the exit slit size. It typically varies from 10–30 μm.

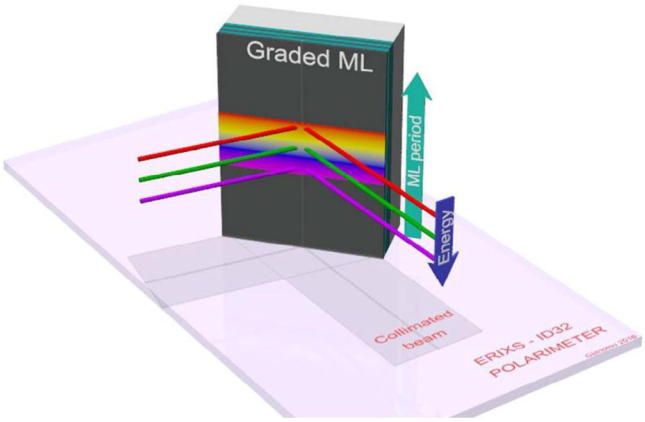

Fig. 23. The polarimeter based on a graded multilayer mirror in a grating spectrometer.

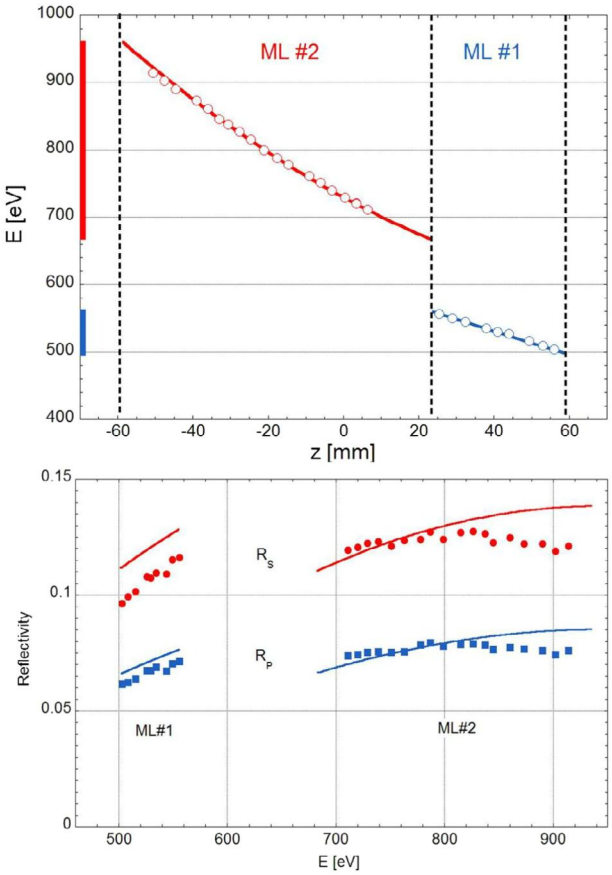

Fig. 24. Upper panel: The correspondence between photon energy and position (z) on the multilayers (ML), as calculated for $\theta = 20°$, with the period d ranging linearly in z from 3.75 nm to 3.32 nm going from 498 eV to 559 eV in ML1, and from 2.77 nm to 1.91 nm for the 667–960 eV interval. Lower panel: The expected (lines) and measured reflectivity (points) over the whole energy range of the polarimeter.

Having such a high energy resolution allows new features to be resolved. An example is shown in Fig. 26 where a phonon is resolved at <60 meV from the elastic peak [42]. This was measured at the Cu L_3 edge at 20 K from an underdoped $Nd_{1.2}Ba_{1.8}Cu_3O_{6+\delta}$ superconductor with a combined energy resolution of ~40 meV.

It is also important when using the polarimeter, which by design works with the 1400 l/mm spectrometer grating, to maintain the sample energy resolution as for the direct photon beam. This is illustrated in Fig. 27 where elastic peaks are measured from carbon tape both for the direct and the beam after reflection by the polarimeter on the

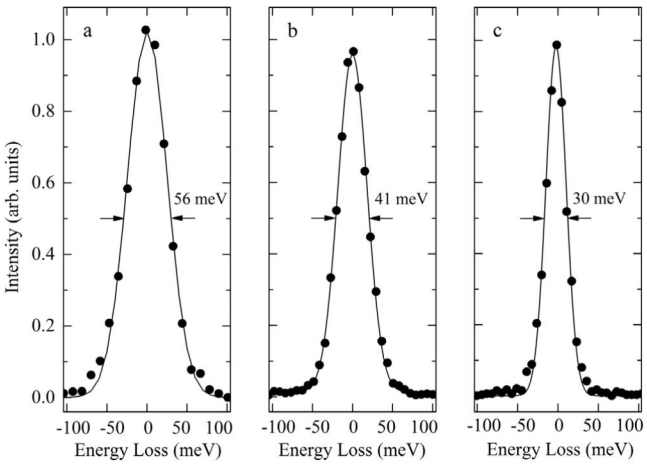

Fig. 25. Elastically scattered X-ray beam (932 eV) from a carbon tape showing the achieved energy resolution (FWHM) for (a) 800 l/mm + 1400 l/mm (b) 800 l/mm + 2500 l/mm and (c) 1600 l/mm + 2500 l/mm, beamline and ERIXS spectrometer grating settings respectively. The lines are Gaussian fits to the data points.

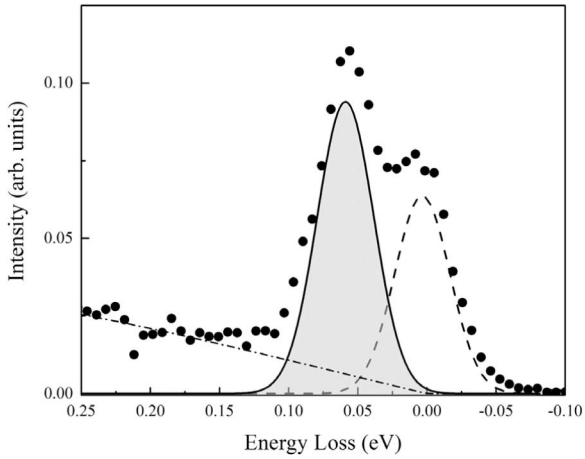

Fig. 26. RIXS spectrum from underdoped $Nd_{1.2}Ba_{1.8}Cu_3O_{6+\delta}$ at $Q_{\parallel} = 0.4$. The phonon is shaded.
Source: Adapted from Ref. [42].

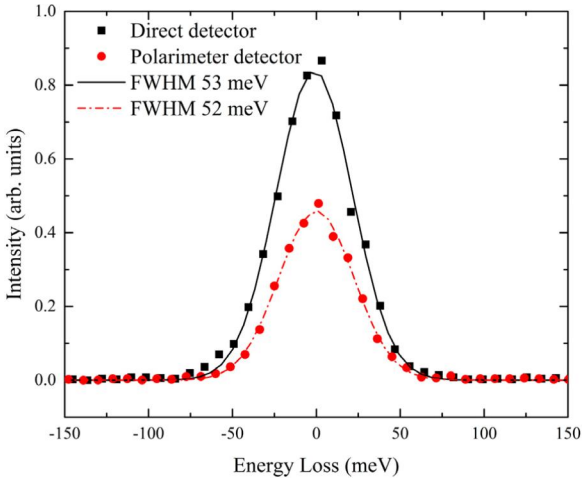

Fig. 27. Elastically scattered X-rays from a carbon tape showing the beam shape measured with the direct (black squares) and the polarimeter (red circles) detectors at a photon energy of 832 eV. The lines are Gaussian fits to the data.

polarimeter detector. As can be seen the energy resolution and peak shapes are essentially the same in both cases. The Gaussian fits give peak widths of 52–53 meV.

10. Beamline diagnostic tools

Having the correct beam diagnostic tools for visualising the beam and commissioning each element in the beamline is critical to the success of a modern state-of-the art synchrotron beamline. ID32 uses a combination of screen monitors, variable slits, intensity monitors and spectral characterisation tools.

The imaging screen monitors include the DiagOn (see Section 3), for aligning the undulators, as well as high power and low power screen monitors (before and after the monochromator respectively). The pre-monochromator beam monitors are water cooled CVD diamond screens where the luminescence is visualised using an in air CCD camera. The screen is moved into the beam to visualise and out during measurements. It gives the position, beam size and shape. The same monitor is used after the monochromator but with a YAG:Ce single crystal screen instead of the diamond. This gives off visible light when illuminated by soft X-rays. The beam viewers were developed in-house [43] for hard X-ray applications but work well in the soft X-ray range as well. The field of view is 12 mm and the pixel size 20 μm.

For visualising the sample at the XMCD high field magnet end station a mirror is permanently positioned in the vacuum tube before the sample chamber (Fig. 2, XMCD branch, position #1). It has a 3 mm hole to allow the beam to pass and is inclined at 45° so that a CCD camera positioned vertically above the mirror can image the sample through a view port. The field of view is 50 mm and the pixel size 56.5 μm. The beam images shown in Fig. 6 were taken with this camera by placing a YAG:Ce screen at the sample position.

To visualise the beam size at the RIXS sample position, razor blades (horizontal and vertical) are placed at the sample position. The beam can be profiled using an edge scan. A YAG:Ce screen can also be positioned at the sample position and viewed with an out of vacuum CCD camera. This only gives the beam position but does not have the resolution to measure the beam size or shape.

Various intensity monitors are also available:

The total luminescent yield from the diamond monitor crystals can be used by integrating the intensity on the CCD imaging cameras. In addition, the diamond screen monitors have a silicon diode detector to measure the scattered X-rays and give an intensity measurement.

The deflecting mirror after the monochromator on the XMCD branch and the final mirrors before the sample on both branches are also electrically isolated so that the drain current from the mirror can be used as an intensity monitor.

In addition, reference samples are situated after the exit slit, see Fig. 2. Several pellets can be selected using a horizontal linear drive. Typically a pellet would have a series of transition metal oxides or rare-earth oxides to cover the edges typically used in experiments. The reference sample is positioned using a linear drive to intercept the edge of the X-ray beam and the drain current is measured. The signal can be taken in parallel with measurements in the sample chamber so that energy drifts can be monitored and if needed corrected for. On the same linear drive is a 100 mm^2 AXUV100 silicon diode detector (IRD photodiode, Opto Diode Corp.) for total intensity measurements.

On the XMCD branch there is an I0 situated after the final mirror and sample slits but before the sample chamber. It is mounted on a linear and rotary drive. The I0 is either a high density (1500 l/inch, Precision Eforming) gold grid (18% transmission) or a thin (~150 nm) boron doped self-standing diamond film as described elsewhere [44]. In both cases the total electron yield is measured. The I0 monitor is situated far (~2 m) from the high field magnet to avoid field effects on the I0 electron yield. In this way it is also in the defocused beam which means more lines are sampled by the grid which is better for linearity. The I0 chamber contains a gold evaporator to evaporate fresh gold onto the

grid to give a homogeneous yield and avoid contamination signals from the grid. On the same linear drive is also a 100 mm^2 AXUV100 silicon diode detector (IRD photodiode, Opto Diode Corp.) for total intensity measurements.

Provision for an I0 monitor after the final mirror has been made on the RIXS branch but it has not been implemented to date. Instead the drain current from the mirror is measured. The intensity of the beam in the RIXS chamber can be measured using an AXUV100 silicon diode detector (IRD photodiode, Opto Diode Corp.) which is installed on the scattering arm and can be moved to intercept the direct beam.

In addition to the reference samples the energy scale can be calibrated using a gas cell situated after the exit slit on both branches. A mixture of neon and nitrogen gas gives access to the absorption edges at ~872 eV and ~401 eV respectively. In addition to checking the energy resolution as described above, the position of the peaks are well known and can be used to calibrate the energy scale of the monochromator. The gas cell is permanently in the beam line and can be easily used by closing a valve after the cell and a window valve (Al foil 100 nm thick) before the cell. The cell is in the beamline vacuum tube and is composed of two plates in the horizontal plane. Gas is introduced at 10^{-4} mbar and the ion or electron current is measured from one of the plates. The other plate is biased at ~1000 V. Once the measurements have been done a turbo pump pumps away the gas and the pressure recovers rapidly so that the valves can be re-opened for normal operation. Having knowledge of the energies from the gas phase absorption spectra, the positions of the absorption peaks from the reference samples and also the XMCD zero-order position of the monochromator allows an accurate calibration of the monochromator energy scale.

Another important aid in commissioning the beamline and diagnosing problems are movable beamline slits. In Fig. 2 it can been seen that before every optical element there is a variable slit. Most are in both horizontal and vertical plane, but some are only in one. By being able to selectively illuminate parts of an optical element it is easier to optimise the alignment. For example with a bent mirror each part of the mirror should give an image at the same point and if it does not the bender can be adjusted for the optimal focus. Also commissioning the gratings is aided by being able to select different parts of the grating and checking the energy and resolution at each point. Most of the slits are open during real measurements. The exceptions are the primary slits which define the undulator emission accepted, the secondary slits which define the horizontal acceptance of the first mirror and the final slits before the sample which can be used to define the beam at the sample position. More sophisticated methods such as wave-front propagation can give more accurate information but were not found necessary to achieve the desired beamline performance.

11. Conclusions and prospective

With regards to the XMCD branch of the ID32 soft X-ray beamline, it has been open to users since October 2014 [29,45–49]. The initial objectives of providing a state-of-the art soft X-ray absorption beamline which is easy to use and allows for a variable spot size at the sample and focussed beams in two experimental areas have been achieved. Together with the extensive sample preparation facility [28] ID32 provides experimenters with up-to-date facilities for today's challenging soft X-ray dichroism experiments. The optical scheme has not been used for such applications before but it has many advantages, in particular its flexibility and ease of use.

The RIXS branch of the ID32 soft X-ray beamline has been open to users since July 2015 [42,50,51]. The aim of achieving 30 000 resolving power at 930 eV has been achieved. Together with the very high energy resolution, the flexible sample environment, with a four-circle goniometer and a scattering arm that can move continuously over 100° has opened up many new possibilities.

Future improvements of the energy resolution could include reducing the spot size at the sample (towards 1 μm), improving the optical quality of the gratings (< = 0.1 μrad rms) and possibly better (faster read out, optimised spatial resolution) detectors. Such improvements could potentially improve the resolving power by a factor of 2 or more. It is also planned to improve the efficiency for total fluorescence yield measurements by adding a CsI coated multichannel plate (MCP) detector on the scattering arm in the RIXS sample chamber as has been done elsewhere [e.g. Ref. [52]].

In 2019, the ESRF will enter a shutdown for the Extremely Bright Source (EBS) upgrade of the accelerator complex (ESRF Upgrade Programme Phase II, 2014). Since the straight section will be reduced from 6 m to 5 m the undulators will need to be reconfigured with the two 1.6 m undulators being probably replaced by a 2.1 m undulator together with the existing 2.5 m undulator. Overall the flux from the beamline is expected to be very similar after the upgrade. In addition, due to the improved beam emittance, the horizontal beam size at the sample position will be reduced; however, the most significant change will be the increased coherent fraction in the soft X-ray range. For example, at 700 eV it will increase by a factor of 10 to ~45% for a 4 m, 88 mm period helical undulator [9]. This may mean more demand for coherent experiments particularly in the open experimental area on the XMCD branch.

Finally, new and improved beamlines are still being realised around the world. In particular, with the push for facilities for very high energy resolution soft X-ray RIXS this will in the near future result in new instruments in Sweden [53], Taiwan [54], the UK and the USA [55], with other projects in the planning stages. Consequently, a bright future for research based on these types of instrumentations is seen for the coming years.

Acknowledgments

The RIXS spectrometer and polarimeter were jointly designed by the ESRF and the Politecnico di Milano. GG acknowledges the support of the MIUR Italian Ministry for Research through project PIK Polarix.

We would like to express our thanks to the Technical Design Review panel members:

J. Nicolás, P. Ohresser, G. Rossi, J.-E. Rubensson, V. Strocov and J. Viefhaus for their invaluable comments.

The help of R. Reininger's with the initial design study is also greatly appreciated.

We would like to thank W.-S. Lee for providing the raw data for Fig. 26.

In addition, we would like to acknowledge the input of many other people, in particular:

R. Baker, J. Chavanne, G. Dellea, M.-C. Dominguez, P. Feder, E. Jimenez Romero, M. Leme, M. Medeiros Soares, M. Minola, C. Morawe, M. Sanchez del Rio, V. Sessi, P. Thakur and A. Vivo.

References

[1] Science and Technology Programme 2008–2107. http://www.esrf.fr/UsersAndScience/Publications/Highlights/2008/upgrade-programme-report.
[2] F. de Groot, A. Kotani, Core Level Spectroscopy of Solids, CRC Press, 2008.
[3] L.J.P. Ament, M. van Veenendaal, T.P. Devereaux, J.P. Hill, J. van den Brink, Rev. Modern Phys. 83 (2011) 705.
[4] G. Ghiringhelli, A. Piazzalunga, C. Dallera, G. Trezzi, L. Braicovich, T. Schmitt, V.N. Strocov, R. Betemps, L. Patthey, X. Wang, M. Grioni, Rev. Sci. Instrum. 77 (2006) 113108.
[5] V.N. Strocov, T. Schmitt, U. Flechsig, T. Schmidt, A. Imhof, Q. Chen, J. Raabe, R. Betemps, D. Zimoch, J. Krempasky, X. Wang, M. Grioni, A. Piazzalungaa, L. Patthey, J. Synchrotron Radiat. 17 (2010) 631.
[6] T. Schmitt, V.N. Strocov, Ke-Jin Zhou, J. Schlappa, C. Monney, U. Flechsig, L. Patthey, J. Electron Spectrosc. Relat. Phenom. 188 (2013) 38.
[7] S. Sasaki, K. Kazunori, T. Takada, T. Shimada, K. Yanagida, Y. Miyahara, Nucl. Instrum. Methods A 331 (1993) 763.
[8] J. Chavanne, P. Elleaume, P. Van Vaerenbergh, Proc. Particle Accelerator Conference, 1999, p. 2565.
[9] ESRF Upgrade Programme Phase II (2015-2022) - Technical Design Study, 2014. http://www.esrf.fr/Apache_files/Upgrade/ESRF-orange-book.pdf.

[10] K. Desjardins, S. Hustache, F. Polack, T. Moreno, M. Idir, J.-M. Dubuisson, J.-P. Daguerre, J.-L. Giorgetta, S. Thoraud, S.F. Delmotte, M.-F. Ravet-Krill, AIP Conf. Proc. 879 (2007) 1101.

[11] J. Chavanne, 2016. Private communication.

[12] Ph. Marion, F. Comin, G. Rostaing, M. Nicola, L. Eybert, MEDSI-PROC-04-42, 2004.

[13] L. Zhang, R. Barrett, K. Friedrich, P. Glatzel, M. Mairs, P. Marion, G. Monaco, C. Morawe, T. Weng, J. Phys. Conf. Ser. 425 (2013) 052029-1.

[14] H. Petersen, H. Baumgartel, Nucl. Instrum. Methods 172 (1980) 191.

[15] J.S. Shah, M.E. Straumanis, Solid State Commun. 10 (1972) 159.

[16] L. Zhang, M. Sanchez del Rio, G. Monaco, C. Detlefs, T. Roth, A.I. Chumakov, P. Glatzel, J. Synchrotron Radiat. 20 (2013) 567.

[17] C. Chauvet, F. Polack, M.G. Silly, B. Lagarde, M. Thomasset, S. Kubsky, J.P. Duval, P. Risterucci, B. Pilette, I. Yao, N. Bergeard, F. Sirotti, J. Synchrotron Radiat. 18 (2010) 761.

[18] P. Risterucci, G. Held, A. Bendounan, M.G. Silly, C. Chauvet, D. Pierucci, N. Beaulieu, F. Sirotti, J. Synchrotron Radiat. 19 (2012) 570; F. Sirotti, Private communication.

[19] M.R. Howells, U. Staub, PSI Bericht Nr. 96-20, 1996. http://www.iaea.org/inis/collection/NCLCollectionStore/_Public/28/047/28047101.pdf.

[20] E. Pereiro, J. Nicolas, S. Ferrer, M.R. Howells, J. Synchrotron Radiat. 16 (2009) 505.

[21] F. Schafers, M. Krumrey, Technischer Bericht, BESSY TB 201, 1, 1996.

[22] B. Nelles, DIOS, private communication.

[23] O. Hignette, P. Cloetens, G. Rostaing, P. Bernard, C. Morawe, Rev. Sci. Instrum. 76 (2005) 063709-1.

[24] K.C. Prince, R.R. Blyth, R. Delaunay, M. Zitnik, J. Krempasky, J. Slezak, R. Camilloni, L. Avaldi, M. Coreno, G. Stefani, C. Furlani, M. de Simone, S. Stranges, J. Synchrotron Radiat. 5 (1998) 565.

[25] M. Sanchez del Rio, N. Canestrari, F. Jiang, F. Cerrinac, J. Synchrotron Radiat. 18 (2011) 708.

[26] O. Chubar, P. Elleaume, Proc. of the EPAC98 Conference, 1998, p. 1177.

[27] B.L. Henke, E.M. Gullikson, J.C. Davis, At. Data Nucl. Data Tables 54 (1993) 181.

[28] K. Kummer, A. Fondacaro, E. Jimenez, E. Velez-Fort, A. Amorese, M. Aspbury, F. Yakhou-Harris, P. van der Linden, N.B. Brookes, J. Synchrotron Radiat. 23 (2016) 464.

[29] N. Bukin, C. McKeever, E. Burgos-Parra, P.S. Keatley, R.J. Hicken, F.Y. Ogrin, G. Beutier, M. Dupraz, H. Popescu, N. Jaouen, F. Yakhou-Harris, S.A. Cavill, G. van der Laan, Sci. Rep. 6 (2016) 36307-1.

[30] T. Harada, M. Itou, T. Kita, SPIE 503 (1984) 114.

[31] R. Reininger, A.R.B. de Castro, Nucl. Instrum. Methods A 538 (2005) 760.

[32] R. Reininger, K. Kriesel, S. Hulbert, C. Sanchez-Hanke, D. Arena, Rev. Sci. Instrum. 79 (2008) 033108.

[33] R. Reininger, Nucl. Instrum. Methods A 649 (2011) 139.

[34] W.B. Peatman, Gratings, Mirrors and Slits: Beamline Design for Soft X-Ray Synchrotron Sources, Gordon and Breach, 1997.

[35] F. Riemer, R. Torge, Nucl. Instrum. Methods 208 (1983) 313.

[36] T. Schmitt, V.N. Strocov, J. Raabel, T. Schmidt, U. Flechsii, C. Dallera, G. Ghiringhelli, A. Imhof, B. Jakob, C. Vollenweider, V. Schonherr, Q. Chen, R. Betemps, J. Krempaski, X. Wang, L. Braicovich, M. Grioni, L. Patthey, J. Electron Spectrosc. Relat. Phenom. 156 (2007) 69.

[37] L. Braicovich, M. Minola, G. Dellea, M. Le Tacon, M. Moretti Sala, C. Morawe, J.-C. Peffen, R. Supruangnet, F. Yakhou, G. Ghiringhelli, N.B. Brookes, Rev. Sci. Instrum. 85 (2014) 115104.

[38] M. Dinardo, A. Piazzalunga, L. Braicovich, V. Bisogni, C. Dallera, K. Giarda, M. Marcon, A. Tagliaferri, G. Ghiringhelli, Nucl. Instrum. Methods Phys. Res. A 570 (2007) 176.

[39] C. Dallera, E. Puppin, A. Fasana, G. Trezzi, N. Incorvaia, L. Braicovich, N.B. Brookes, J.B. Goedkoop, J. Synchrotron Radiat. 3 (1996) 231.

[40] A. Amorese, G. Dellea, L. Braicovich, G. Ghiringhelli, 2014, arXiv:1410.1587.

[41] C. Morawe, J.-C. Peffen, R. Supruangnet, L. Braicovich, N.B. Brookes, G. Ghiringhelli, F. Yakhou-Harris, Proc. SPIE 9207 (2014) 92070J.

[42] L. Chaix, G. Ghiringhelli, Y.Y. Peng, M. Hashimoto, B. Moritz, K. Kummer, N.B. Brookes, Y. He, S. Chen, S. Ishida, Y. Yoshida, H. Eisaki, M. Salluzzo, L. Braicovich, Z.-X. Shen, T.P. Devereaux, W.-S. Lee, Nat. Phys. (2017) 10.1038.

[43] T. Mairs, P. Fajardo, J. Meyer, E. Mitchell, D. Nurizzo, V. Rey-Bakaikoa, W. Shepard, O. Svensson, MEDSI-PROC-04-52, 2005.

[44] K. Kummer, A. Fondacaro, F. Yakhou-Harris, V. Sessi, P. Pobedinskas, S.D. Janssens, K. Haenen, O.A. Williams, J. Hees, N.B. Brookes, Rev. Sci. Instrum. 84 (2013) 035105.

[45] A.I. Figueroa, G.E. Campillo, A.A. Baker, J.A. Osorio, O.L. Arnache, G. van der Laan, Superlattices Microstruct. 87 (2015) 42.

[46] A.I. Figueroa, A.A. Baker, S.E. Harrison, K. Kummer, G. van der Laan, T. Hesjedal, J. Magn. Magn. Mater. 422 (2017) 93.

[47] A.A. Baker, A.I. Figueroa, K. Kummer, L.J. Collins-McIntyre, T. Hesjedal, G. van der Laan, Phys. Rev. B 92 (2015) 094420-1.

[48] F. Donati, S. Rusponi, S. Stepanow, C. Wäckerlin, A. Singha, L. Persichetti, R. Baltic, K. Diller, F. Patthey, E. Fernandes, J. Dreiser, Ž. Šljivančanin, K. Kummer, C. Nistor, P. Gambardella, H. Brune, Science 352 (2016) 318.

[49] M. Perfetti, M. Serri, L. Poggini, M. Mannini, D. Rovai, P. Sainctavit, S. Heutz, R. Sessoli, Adv. Mater. 28 (2016) 6946.

[50] Y.Y. Peng, M. Salluzzo, X. Sun, A. Ponti, D. Betto, A.M. Ferretti, F. Fumagalli, K. Kummer, M. Le Tacon, X.J. Zhou, N.B. Brookes, L. Braicovich, G. Ghiringhelli, Phys. Rev. B 94 (2016) 184511-1.

[51] Y.Y. Peng, G. Dellea, M. Minola, M. Conni, A. Amorese, D. Di Castro, G.M. De Luca, K. Kummer, M. Salluzzo, X. Sun, X.J. Zhou, G. Balestrino, M. Le Tacon, B. Keimer, L. Braicovich, N.B. Brookes, G. Ghiringhelli, Nat. Phys. 13 (2017) 1201.

[52] D.G. Hawthorn, F. He, L. Venema, H. Davis, A.J. Achkar, J.R. Zhang, R. Sutarto, H. Wadati, A. Radi, T. Wilson, G. Wright, K.M. Shen, J. Geck, H. Zhang, V. Novák, G.A. Sawatzky, Rev. Sci. Instrum. 82 (2011) 073104-1.

[53] S. Urpelainen, C. Såthe, W. Grizolli, M. Agåker, A.R. Head, M. Andersson, S.-W. Huang, B.N. Jensen, E. Wallén, H. Tarawneh, R. Sankari, R. Nyholma M. Lindberg, P. Sjöblom, N. Johansson, B.N. Reinecke, M.A. Arman, L.R. Merte, J. Knudsen, J. Schnadt, J.N. Andersen, F. Hennies, J. Synchrotron Radiat. 24 (2017) 344.

[54] C.H. Lai, H.S. Fung, W.B. Wu, H.Y. Huang, H.W. Fu, S .W. Lin, S.W. Huang, C.C. Chiu, D.J. Wang, L.J. Huanga T.C. Tseng, S.C. Chung, C.T. Chena, D.J. Huang, J. Synchrotron Radiat. 21 (2014) 325.

[55] J. Dvorak, I. Jarrige, V. Bisogni, S. Coburn, W. Leonhardt, Rev. Sci. Instrum. 87 (2016) 115109.